Bauer Susanne, E. (Orcid ID: 0000-0001-7823-8690)
Tsigaridis Kostas (Orcid ID: 0000-0001-5328-819X)
Faluvegi Greg (Orcid ID: 0000-0001-9011-3663)
Miller Ron, L. (Orcid ID: 0000-0003-2122-0443)
Nazarenko Larissa, S. (Orcid ID: 0000-0003-3172-9358)
Schmidt Gavin, A. (Orcid ID: 0000-0002-2258-0486)

Historical (1850-2014) aerosol evolution and role on climate forcing using the GISS ModelE2.1 contribution to CMIP6

Susanne E. Bauer[1], Kostas Tsigaridis[2,1], Greg Faluvegi[2,1], Maxwell Kelley[3,1], Ken K. Lo[3,1], Ron L. Miller[1], Larissa Nazarenko[2,1], Gavin A. Schmidt[1], Jingbo Wu[4,1]

[1] NASA Goddard Institute for Space Studies, New York, New York

[2] Center for Climate Systems Research, Columbia University, New York, New York

[3] SciSpace LLC, New York NY

[4] Department of Applied Physics and Applied Mathematics, Columbia University, New York NY

Corresponding author: Susanne Bauer (Susanne.E.Bauer@NASA.gov)

Key Points:

- Discussion of the AMIP aerosol simulations for the years 1850 to 2014 of the GISS ModelE2.1 for CMIP6, using two different aerosol schemes.
- Detailed treatment of aerosol microphysical processes greatly impacts aerosol forcing as well as forcing trends.
- One model suggests that Earth has already exceeded the maximum negative forcing effects of anthropogenic aerosol in the 1980s.

This article has been accepted for publication and undergone full peer review but has not been through the copyediting, typesetting, pagination and proofreading process which may lead to differences between this version and the Version of Record. Please cite this article as doi: 10.1029/2019MS001978

Abstract

The Earth's climate is rapidly changing. Over the past centuries, aerosols, via their ability to absorb or scatter solar radiation and alter clouds, played an important role in counterbalancing some of the greenhouse gas (GHG) caused global warming. The multi-century anthropogenic aerosol cooling effect prevented present-day climate from reaching even higher surface air temperatures and subsequent more dramatic climate impacts. Trends in aerosol concentrations and optical depth show that in many polluted regions such as Europe and the United States of America, aerosol precursor emissions decreased back to levels of the 1950s. More recent polluting countries such as China may have reached a turning point in recent years as well, while India still follows an upward trend. Here we study aerosol trends in the CMIP6 simulations of the GISS ModelE2.1 climate model using a fully coupled atmosphere composition configuration, including interactive gas-phase chemistry, and either an aerosol microphysical (MATRIX) or a mass-based (OMA) aerosol module. Results show that whether global aerosol radiative forcing is already declining depends on the aerosol scheme used. Using the aerosol microphysical scheme, where the aerosol system reacts more strongly to the trend in sulfur dioxide (SO_2) emissions, global peak direct aerosol forcing was reached in the 1980's, whereas the mass-based scheme simulates peak direct aerosol forcing around 2010.

Plain Language Summary

The NASA Earth system model, GISS ModelE2.1, has released new interactive composition climate simulations from 1850 to 2014 into the Coupled Model Intercomparison Project Phase 6 (CMIP6) Diagnosis, Evaluation, and Characterization of Klima protocol archive. The GISS model includes two different schemes to simulate aerosols in the atmosphere, driven by natural and anthropogenic emissions. The two aerosol schemes differ by degree of complexity. One model better resolves aerosol microphysical processes, while the other model has more detailed chemistry regarding secondary organic aerosol formation. The models simulate different trends in aerosol radiative forcing. An evaluation with satellite data between 2001 and 2014 demonstrates that the model with more detailed aerosol microphysics has reached maximal aerosol direct forcing in the 1980s, and is since on a decreasing global forcing trajectory. This has implications for using the trends over recent decades as predictive for greenhouse-gas related changes in the future.

1 Introduction

Aerosols and clouds have been on the forefront of climate research for decades (Hansen et al., 1998) and our understanding of the role of aerosols as climate forcers has increased significantly over the past years. Nevertheless, uncertainties are still extremely high compared to other forcers of the climate system. Observational constraints for the aerosol direct radiative forcing, the anthropogenic component of the aerosol direct radiative effect, are highly uncertain (Bellouin et al., 2005, 2008; Su et al., 2013), which contributes to the large spread in forcing estimates for 2000 relative to 1850 (−0.02 to −0.58 Wm^{-2}, Myhre et al., 2013)). Modeling aerosol radiative forcing is difficult due to the very complex nature of aerosols themselves, both due to their fast-changing chemical composition and size distribution, but also due to the complex interaction of aerosols with radiation and their impact on cloud macro- and micro-physics. Additional large sources of uncertainty are emissions, natural and anthropogenic, and their evolution over time, which affect the spatiotemporal aerosol distribution in the atmosphere. The question about aerosol effects on climate is as urgent as ever, especially since many models are reporting very high equilibrium climate sensitivity (Gettelman et al., 2019; Golaz et al., 2019), as well as difficulties in matching the historical temperature record with transient climate models (Gettelman et al., 2019; Golaz et al., 2019; Held et al., 2020; Sellar et al., n.d.; Voldoire et al., 2019). As such understanding trends in forcing, the drivers of climate change, as well as the performance of the Community Emission Data System (CEDS) in support of CMIP6 (Hoesly et al., 2018) and biomass burning emission (van Marle et al., 2017) that are used by the entire climate modeling community, is timely. Understanding composition trends over the entire historical simulation period, 1850 to 2014, is challenging, and only ice core records can be used to reconstruct aerosol information over such long timescales. During the last decades a larger number of measurements of aerosol concentrations have been made available from surface, suborbital and orbital platforms. Especially over the last two decades when the MODerate resolution Imaging Spectroradiometer (MODIS) and Multi-angle Imaging SpectroRadiometer (MISR) instruments started orbiting Earth, a wealth of information has become available which helped us promote our understanding of aerosol occurrence and evolution in the Earth's atmosphere (Alfaro-Contreras et al., 2017; Fan et al., 2018; Hu et al., 2018; Levy et al., 2010, 2013, 2015; Oikawa et al., 2018; Sayer et al., 2014). Through those studies, the emission-control measures that led to the cleaning of air over the US and Europe, together with the pollution increase that followed the explosion of industrial activity in South and East Asia, quickly became apparent (Adesina et al., 2016; Aklesso et al., 2018; Arkian &

Nicholson, 2017; Boiyo et al., 2018; Floutsi et al., 2016; Gopal et al., 2016; He et al., 2016; Jongeward et al., 2016; Kumar et al., 2018; Mehta et al., 2018; Shokr et al., 2017; Wang et al., 2017, 2016; Xu et al., 2015). As such satellite retrieved aerosol optical depth (AOD) can be used for trend studies, changes in clear-sky shortwave radiative fluxes constrained by the observed variability in outgoing shortwave radiation from the Clouds and the Earth's Radiant Energy System (CERES) can be used to look at radiative flux trends over the past two decades (Paulot et al., 2018).

In addition to the trend analysis, in this work we aim to give a detailed description of the aerosol configurations of the GISS ModelE2.1 historical Atmospheric Model Intercomparison Project (AMIP) simulations. We study the effect of the microphysical aerosol scheme, MATRIX, against the mass-based aerosol scheme, OMA, both in terms of AOD and forcing. The OMA model, which is the new name of the aerosol model developed at GISS since Tegen & Fung (1994) and Koch et al. (1999) and is still under active development, (e.g. Perlwitz et al., 2015a), has been used for ozone and aerosol simulations with the GISS model for CMIP3 (Hansen et al., 2000), CMIP5 (Schmidt et al., 2014) and CMIP6. This is particularly important, since the OMA monthly-mean output is used as offline fields to drive GISS ModelE2.1 in all historical and climatological non-interactive atmospheric composition simulations for CMIP6.

This paper is organized as follows. In section 2, we describe the climate model components, with a specific focus on the two aerosol schemes, and the evaluation data sets. In section 3 results are presented for the global trends from 1850 to 2014 in forcing and composition (3.1), a model comparison with ice cores (3.2), a regional analysis of composition and forcing (3.3), and a global model-satellite trend analysis between 2001 and 2014 (3.4). Finally, we present a summary of the historical aerosol simulations in section 4 and draw conclusions in section 5.

2 Methodology

2.1 The Climate Model

A full description of ModelE2.1 and evaluation of its coupled climatology during the satellite era (1979–2014) and the historical ensemble simulation of the atmosphere and ocean component models (1850-2014) are under preparation. The model we are describing here is the AMIP composition simulation (GISS, 2019) (https://doi.org/10.22033/esgf/cmip6.6986) of ModelE2.1 with prescribed sea surface temperature (SST) and sea ice fraction during the historical period (Rayner et al., 2003). The horizontal and vertical resolution of the

atmospheric ModelE2.1 is 2° in latitude by 2.5° in longitude with 40 vertical layers extending from the surface to 0.1 hPa in the lower mesosphere.

Here, aerosols and ozone are calculated prognostically using either the One-Moment Aerosol (OMA) or the MATRIX model ('Multiconfiguration Aerosol TRacker of mIXing state'). The OMA version is designated as physics-version 3 ('p3') in the CMIP6 archive to signify continuity with its CMIP5 predecessor named TCADI in pre-CMIP6 publications. The MATRIX version of ModelE2.1 is designated as physics-version ('p5'). The following archive numbers identify the five ensemble simulations per model configuration, GISS-E2-1-G_amip_r[1-5]i1p5f1 (MATRIX) and GISS-E2-1-G_amip_r[1-5]i1p3f1 (OMA). The monthly aerosol and ozone fields of the simulations of the OMA model, presented here, are used to drive all other simulations of the GISS model for CMIP6, that do not include online interactive chemistry and aerosols, denoted as NINT (for 'non-interactive') in the CMIP6 archive as physics-version 1 ('p1').

Both aerosol schemes are coupled to the tropospheric chemistry scheme (Shindell et al., 2001, 2003), which includes inorganic chemistry of O_x, NO_x, HO_x, CO, and organic chemistry of CH_4 and higher hydrocarbons using the CBM4 scheme (Gery et al., 1999), and the stratospheric chemistry scheme (Shindell et al., 2006) which includes chlorine and bromine chemistry together with polar stratospheric clouds.

MATRIX (Bauer et al., 2008, 2010a; Bauer & Menon, 2012), is an aerosol microphysics scheme based on the quadrature method of moments. MATRIX represents new particle formation (the binary scheme (Vehkamäki et al., 2002) was chosen here), gas-particle mass transfer, aerosol-phase chemistry, condensational growth, and coagulation within and between particle populations. MATRIX is able to explicitly simulate the mixing state of aerosols (Bauer, Ault, et al., 2013). The amount of water in aerosol is calculated with the aerosol thermodynamics module EQSAM (Metzger et al., 2002), using the phase state of an ammonia-sulfate-nitrate-water inorganic aerosol in thermodynamic equilibrium for metastable aerosols, except for sea salt where the Lewis parameterization is used (Lewis & Schwartz, 2013) is used. As such, hygroscopic swelling of aerosol is already considered and does not need to be recalculated during the radiative calculations. Note, a new functionality related to the explicit treatment of partitioning of semi-volatile organics (Gao et al., 2017, 2018) that is part of MATRIX was not used here, as it was not included in the CMIP6 simulations. In the version used here, secondary organic aerosol (SOA) is parameterized as a source of non-volatile

aerosol emitted directly from vegetation. A 10% yield from monoterpene emissions is assumed, which is added to the non-volatile organic aerosol fraction in the model, and remains indistinguishable from organic aerosols from other sources. MATRIX results presented here use mechanism M1 (Bauer et al., 2008) that tracks 16 mixing state classes, 51 aerosol tracers and resolves eight chemical components; sulfate, nitrate, ammonium, aerosol water, black carbon, organic carbon, sea salt and mineral dust. In MATRIX the number of cloud activating particles is based on the aerosol activation parameterizations of (Abdul-Razzak et al., 1998; Abdul-Razzak & Ghan, 2000), which treat multimodal and multicomponent aerosols and provide the activated fraction for the number and mass concentrations for each population, based on the composition of each population and the cloud updraft velocity. ModelE2.1 only includes the first indirect effect, which is the effect of aerosols on cloud droplet number concentration (CDNC) and thereby on cloud albedo, cloud effective radii and radiation (Menon et al., 2008, 2010).

OMA (Bauer, Koch, et al., 2007; Bauer, Mishchenko, et al., 2007; Bauer & Koch, 2005; Koch et al., 2006; Miller et al., 2006; Tsigaridis et al., 2013), is a mass-based scheme in which aerosols are externally mixed and assumed to have a prescribed constant size distribution. OMA transports 34 tracers. The following aerosol components are treated in this version: sulfate, nitrate, ammonium, carbonaceous aerosols (black carbon and organic carbon, including the NO_x-dependent formation of SOA and methanesulfonic acid formation (Tsigaridis and Kanakidou, (2007)), dust (including heterogeneous gas uptake on dust surfaces (Bauer & Koch 2005)) and sea-salt. Aerosol hydration in OMA is calculated in the radiation code following (Tang & Munkelwitz, 1994). Sea salt has two distinct size classes, and dust that is described by a sectional model with an option of choosing from 4 to 6 bins. The default dust configuration, which is what is used here, includes 5 bins, a clay and 4 silt classes, from submicron to 16 μm in radius. An additional capability of OMA is to simulate the mineralogical composition of dust (Perlwitz et al., 2015a, 2015b), but was not used here. OMA only includes the first indirect effect. The aerosol number concentrations that impact clouds are obtained from the aerosol mass as described in (Menon & Rotstayn, 2006).

The treatment of emissions is identical for both aerosol models. Sea salt, DMS, isoprene and dust emission fluxes are calculated interactively. Anthropogenic dust sources are not represented in ModelE2.1. Dust emissions vary spatially and temporally only with the evolution of climate variables like wind speed and soil moisture (Miller et al., 2006). The

remaining anthropogenic fluxes come from the Community Emissions Data System (CEDS) inventory (Hoesly et al., 2018). Biomass burning comes from either the GFED4s inventory (van der Werf et al., 2017) for the 1997-2014 period or from (van Marle et al., 2017) for the pre-1997 period; both datasets are part of the CEDS inventory. Continuous (effusive) volcanic emissions emit SO_2 in the model, but eruptive volcanoes are prescribed as stratospheric AOD and effective particle size (Arfeuille et al., 2014; Thomason et al., 2018). The latter are only considered in the radiation model, and are not part of the composition simulation in this version of the model. All AMIP ensemble results presented here are the mean of 5 ensemble members that were started from varying initial conditions. The five simulations were performed by starting from the end of a 10-year-long atmospheric control simulation with recurring conditions for the year 1850, which brings the model into compositional equilibrium. Simulations are run from 1850 until the end of 2014. All other forcings follow the CMIP6 protocol.

Before discussing model results, we point to known errors in the CEDS emission inventory (https://github.com/JGCRI/CEDS/wiki/Data_and_Assumptions#known-issues-1) that can impact our results: (a) Combustion emissions are zero in earlier years for several countries, (b) SO_2 emissions in the western US are too high compared to US EPA state emissions data, and (c) SO_2 emissions in the US are overestimated from about 1961 to 1969. The overestimate averages 22% over that eight-year period. In addition, we note that the CEDS biomass burning emission inventories (van Marle et al., 2017; van der Werf et al., 2017) are biased low (Bauer et al., 2019; Mezuman et al., 2019; Pan et al., 2019).

2.2 Observational Datasets

Two MODIS instruments are in space on the Terra and Aqua satellites. Terra crosses the equator southward at 10:30am local time, while Aqua passes northward at 1:30pm. We use the column aerosol optical depth (AOD) at 550 nm observations from Moderate Resolution Imaging Spectroradiometer (MODIS) Collection 6 Dark Target and Deep Blue combined product (Levy et al., 2010). The Dark Target AOD product covers the global oceans and only the dark surfaces of continents like vegetated areas. Some of the Terra data, and all of the Aqua data, have a Deep Blue product, which allows retrievals over additional land surface types.

The Clouds and the Earth's Radiant Energy System (CERES; Wielicki et al., 1998) provides measurements of the Earth's radiative budget since 2000. Here, we use the Energy Balanced

and Filled product (EBAF, edition 4; Loeb et al., 2018) to estimate the variability of the clear-sky shortwave outgoing radiation. This product achieves global coverage by combining CERES broadband cloud-free fluxes with MODIS radiances for regions that are not completely cloud-free at the CERES footprint scale (Loeb et al., 2018).

Surface aerosol data are measured by the Interagency Monitoring of Protected Visual Environments (IMPROVE) network over the United States (Malm et al., 1994, 2004), and by the European Monitoring and Evaluation Program (EMEP, www.emep.int), available via the NILU-EBAS database for Europe. IMPROVE currently has 212 sites, predominantly rural (Hand et al., 2012), while EMEP has around 40 sites measuring aerosol composition in Europe.

This study uses six ice core records for sulfate and black carbon inclusions. Three cores are from high latitude locations in Greenland and Spitzbergen, and three cores are from the mid latitudes. The two Greenland ice cores are NEEM, a 411 m deep ice core drilled in 2011 at 77°45'N, 51°06' W at 2454 m a.s.l. in northwest Greenland (Sigl et al., 2013), and the Summit core located further east at 72°36'N, 38°18'W at 3258m a.s.l. (Keegan et al., 2014). The ice core from Spitzbergen, Lomonosovfonna, Svalbard, was drilled at 78°49'N, 17°26'E at an elevation of 1202 m a.s.l. (Osmont et al., 2018). The three cores drilled on glaciers in the mid latitudes are: The Colle Gnifetti core, a 82m long ice core from the European Alps (Jenk et al., 2009; Sigl et al., 2018), drilled in 2003 on Colle Gnifetti (Monte Rosa, 4450 m a.s.l., 45°55' N, 07°52' E), the Mongolian ice core, Tsambagarav, at 48°39'N, 90°51'E 4130 m a.s.l. (Herren et al., 2013), and ice cores drilled at a high-altitude eastern European site in Mt. Elbrus, Caucasus (43°21'N, 42°26'E, 5115 m a.s.l.) in Southern Russia near the border to Georgia, covering the period 1825–2013 (Lim et al., 2017). The cores refractory black carbon (rBC) is measured by SP2 (Schwarz et al., 2006) while measurements of ions are performed by the use of ion chromatography (Sigl et al., 2018). All ice core concentration records are converted to deposition fluxes using core melting rates reported in the data sets and cited publications, and are compared to the modeled deposition fluxes on snow.

3 Results

3.1 Global forcing trends

The radiative forcing trends over the past decades differ for the two aerosol modules, MATRIX and OMA, despite the fact that the host model and anthropogenic emissions were identical. We

use instantaneous direct aerosol forcing numbers RFari(i) and cloud forcings (Figure 1a and c) using the diagnostics of the historical transient simulations, based on double calls to the radiation including and excluding aerosol forcing effects. The transient cloud radiative effect follows the definition by Ghan (2013) using the difference in cloud radiative forcing calculated as a diagnostic with aerosol scattering and absorption omitted. In addition, we have performed fixed-SST simulations under present climate conditions but using 1850 emissions, to calculate the effective radiative forcing that includes the effect of rapid adjustments of the atmosphere and land surface upon the initial radiative imbalance (Myhre et al., 2014). Those simulations are used to report aerosol radiation interactions (RFari) and aerosol cloud interaction (RFaci) forcings and are shown in Figure 2.

The global mean RFari(i) anomalies with respect to 1850 (Fig 1a), show the dominance of the cloud forcing over aerosol direct forcing. Using 10-year means around 1850-1859 and 2005-2014, RFari(i) equals -0.17 Wm^{-2} for MATRIX and -0.24 Wm^{-2} for OMA (Fig.1 c), RFari equals to -0.28 Wm^{-2} for MATRIX and -0.31 Wm^{-2} for OMA (Fig. 2). The cloud radiative effect equals to -1.53 Wm^{-2} for MATRIX and -1.85 Wm^{-2} for OMA (Fig. 1a), and RFaci equals -1.08 Wm^{-2} for MATRIX and -1.54 Wm^{-2} for OMA (Fig. 2).

The most striking difference in RFari(i) between OMA and MATRIX in the CMIP6 model are the trends after the 1970s. MATRIX (Fig 1c) shows its strongest direct forcing around 1980s and subsequently decreases back to its 1960s magnitude. In contrast, the OMA model shows its strongest magnitude around the year 2010, with the remaining years of the historical simulation (up to 2014) not enough to conclude whether this marks a trend reversal. Even so the overall global mean difference in RFari(i) is not that large between the two models, -0.17 Wm^{-2} in MATRIX and -0.24 Wm^{-2} in OMA. The fact that they differ allows some expectation that a trend analysis between the two models and observational AOD, clear sky shortwave radiative fluxes and composition measurements can help explain which model performs more realistically, and thus inform us if we have already passed the era of maximum anthropogenic RFari forcing. The spatial distributions of RFari (Figure 2a and b) shows that MATRIX has a stronger negative forcing over the polluted outflow regions over the oceans and positive forcings over parts of North and Central Africa. OMA has stronger negative forcings at the hotspots of aerosol pollution, such as parts of Asia, Europe and the Eastern US. These regional differences lead to a slightly larger magnitude of RFari in OMA compared to MATRIX. The differences in regional aerosol composition will be further discussed in section 3.3.

The global trends in cloud forcing (Figure 1a), caused by all climate change forcers and not only aerosol effects show a similar behavior between OMA and MATRIX until 1990, thereafter

resulting in MATRIX having a smaller magnitude of cloud forcing compared to OMA. That difference can be explained by the temporal evolution of CDNC, shown in Figure 1e. The temporal evolution of CDNC follows the trend of RFari(i). The global distribution of 1850 to 2014 CDNC and RFaci changes (Figure 2c-f) show similar spatial distributions between OMA and MATRIX, but with a larger amplitude in OMA leading to more negative RFaci compared to MATRIX. Note that the physical and algorithmic link between aerosol loads and CDNC is very different between the two models (see section 2). OMA's aerosol conversion into cloud condensation nuclei (CCN) is empirical, while in MATRIX it is based on prognostic aerosol microphysics and cloud updraft velocities. The short explanation of the different trends in CDNC and RFari(i) is a much stronger sulfate aerosol effect in MATRIX compared to OMA (Figure 1d and f), despite identical temporal driving of the SO_2 emissions (Figure 1b).

3.2 Ice core records

The only source of deposition measurements spanning over the entire historical simulation are from ice core records. Here we compare the models to six cores (Fig. 3), three in high latitude locations, at Greenland and Spitzbergen, and three cores from the mid latitudes.

The sulfate time series for the Greenland core (Fig 4), a record dominated by outflow of pollution from North America, shows peak sulfate concentrations around 1970. All model versions and the core show similar trends, while the CMIP6 models show higher concentrations than the CMIP5 model and the core data. It should be considered that Greenland has high elevation with a very complex terrain for the resolution of a global model, and the concentration levels are an order of magnitude smaller than the other cores used here. The internal annual variability between model and core are similar and better resolved in the CMIP6 models that are driven by monthly emission data, whereas CMIP5 used decadal mean monthly emissions. At Svalbard, the core shows higher concentrations in the 1950s that are not present in the models, and also not seen in the other cores from Greenland or Europe, although with a very large variability. However, the second maxima around 1980 is matched by the models, as well as coincides with the other core records. The core with the highest sulfate concentration is Colle Gnifetti, which is located in the European Alps very close to pollution sources. The match between core and models is exceptional, with increasing concentrations in the 1900s and peak concentrations in the 1970s. The core from Mongolia shows a very similar time evolution compared to Colle Gnifetti, but with longer lasting peak concentrations from 1970 to 1990.

The decrease thereafter is linked to the breakdown of Eastern European and Soviet industries toward the end of that period.

Although the comparison between cores and models for sulfate is very good, the black carbon (BC) performance is more challenging (Fig. 5). A couple of important points regarding the BC comparison is that a) the CMIP5 and CMIP6 models differ more substantially in their BC emissions rather than the sulfur dioxide ones, and b) OMA and MATRIX in CMIP6 are very similar. This is caused by the fact that the parameterized e-folding time of hydrophobic to hydrophilic BC in OMA, a proxy for its aging lifetime, has been tuned in the CMIP6 OMA simulation to match that of MATRIX, which does include physically-based aging calculations as part of the aerosol microphysics. This new aging timescale for OMA has been evaluated using ice cores and HIPPO flight campaign data in Bauer et al. (2013).

The models' BC deposition fluxe amounts over Greenland match well with the ice cores, however the decreasing trend since North American deforestation as well as the switch from coal to fossil fuels since the 1900s is not well captured in the CMIP6 models. BC trends in Svalbard are similar between models and core, but with higher concentration levels measured in the core. The three mid-latitude cores, Alps, Mongolia and Caucasus, all show much lower BC concentrations than the models simulate. The core with the largest BC ice core concentration is Elbrus in the Caucasus.

3.3 Regional trends in composition and forcing

Understanding global trends requires a regional analysis. For this purpose, we divided the globe into 12 sub-regions as indicated in Fig 6. The regions were not chosen by country, rather for showing a significant change in either AOD or in forcing between 2001 and 2014: the beginning of measurements from Aqua and Terra and the end of the CMIP6 historical simulation. Figure 6 includes the emission fluxes of the four major anthropogenic and biogenic aerosol precursors, sulfur dioxide, nitric oxide, organic carbon and ammonia, as well as clear-sky AOD and RFari(i) by MATRIX and OMA. Figure 7 shows the aerosol mass loads in both models for the 12 regions. The regions within the US and Europe are compared to trends in surface concentrations (Fig 8) and all regions are compared to trends in satellite-retrieved AOD (Fig 9). Trends are calculated using the least-squares linear regression methodology on the annual average. Regional satellite trends are only provided when there are no temporal gaps in the dataset. Satellite data sampling for model comparison is further explained in section 3.4.

In the continental US (A and B in Fig. 6) anthropogenic emissions started to rise in the late 19th century. Sulfate dioxide emissions, mainly linked to the energy sector and manufacturing, peaked around 1970 – 80 and since then have decreased back to 1900 levels. Note that the sharp jump in SO_2 emissions in the US in 1960 is a bug in the CEDS emissions (see section 2.1). Nitric oxide emissions, a strong indicator of the transportation sector, have retreated at present to roughly 1960 values. Ammonia, whose main source is linked to food production, is the only aerosol precursor that steadily rises throughout the historical period, since no emission control policies are in place and agricultural emissions are strongly tied to population growth. Carbonaceous aerosol precursors of OC and BC (only shown in Fig 1b, but in general closely follow the OC trend), had their highest emissions in the first half of the historical period, driven by deforestation and wood burning. Overall, the aerosol loads in region A and B are dominated by sulfate and organic aerosol (Figure 7). Surface aerosol concentration measurements from the IMPROVE network are available for North America. Fig. 8 shows trends over the regions A and B averaged over 65 and 35 surface stations, respectively. The models are sampled according to the spatial and temporal observational data availability, and a linear regression is used to calculate the trend. Sulfate has a decreasing trend in the US, with a decrease between 2001 and 2014 of -0.4 μg m^{-3} (-1.4 μg m^{-3} in MATRIX, -1.2 μg m^{-3} in OMA) over the Western US and -3.9 μg m^{-3} (-4.0 μg m^{-3} in MATRIX and -3.6 μg m^{-3} in OMA) over the Eastern US. The models simulate the trend in sulfate well in the Eastern US, but overestimate concentrations in the Western US. This is most likely partially linked to siting of IMPROVE stations in National Parks where topography is complicated and varies at scales much smaller than the model grid size. OMA underestimates the seasonal variability in the Eastern US, while MATRIX shows a better performance. Station observations of carbonaceous aerosols show a weak trend over the 14-year time period, with -1.0 μg m^{-3} in OC and -0.2 μg m^{-3} in BC in the Western and -0.2 μg m^{-3} in OC and -0.3 μg m^{-3} in BC in the Eastern US. The models show almost no trend in carbonaceous aerosols. In terms of concentrations, the OMA OC simulation captures the mean as well as seasonal and interannual variability, while MATRIX overestimates OC, especially in summer concentrations. This version of MATRIX doesn't resolve the organic aerosol (OA) semi-volatile nature, a not so uncommon omission in global models (Tsigaridis et al., 2014). As such, MATRIX overestimates OA concentrations in the summer months, when more organics should partition into the gas phase. Secondary organic aerosol partitioning is included in the OMA model (Tsigaridis & Kanakidou, 2003). The magnitude of clear-sky AOD (Fig 9) is better simulated using MATRIX than OMA when

compared to MODIS, especially over the Eastern US, where the sulfate aerosol simulation was much better captured by the MATRIX model. A difference in the model's clear-sky AOD can be caused by the difference in aerosol hydration calculations between OMA and MATRIX (see section 2). In both schemes, clear-sky AOD is calculated by accumulating AOD only under clear-sky conditions, defined as the absence of clouds in the model column at each model timestep. The seasonal and interannual variability in AOD over the continental US (Fig 6a and b) is similar between the models over the Western US, and much stronger in MATRIX over the Eastern US, in accordance with the sulfate simulation as well as the time evolution of the regional SO_2 emissions.

In Europe (Fig. 6d), SO_2 emissions show a sharp increase after 1950 and a similar decrease since 1980. AOD and RFari(i) largely follow this trend. Major components of aerosol composition in Europe are mineral dust, sulfate, organic aerosol and nitrate (Figure 7), however the AOD and RFari(i) trends are mainly driven by sulfate. Surface sulfate aerosol concentration, based on 25 stations, (Fig. 8) shows a trend of -2.5 $\mu g\ m^{-3}$ (-2.0 $\mu g\ m^{-3}$ MATRIX, -1.5 $\mu g\ m^{-3}$ OMA) over 14 years and this coincides with a decreasing trend in AOD (Fig. 9). MATRIX shows a better simulation of sulfate concentrations and AOD, for reasons similar to what has been discussed for the Eastern US.

Over the Arabian Peninsula (Fig 6. h) an increasing magnitude of AOD and RFari(i) is simulated since 1950, mostly driven by SO_2 emissions, with a weak indication that a maximum was reached around the year 2010. The aerosol load in region H (Fig 7) is dominated by mineral dust, which shows a decreasing trend over the historical simulation. In this region, dust aerosols are an important contributor to AOD, and decreased dust emission over Iraq and an increase over Oman are possibly connected to increased and decreased irrigation in these two regions, respectively, as well as broader changes to the Asian Summer Monsoon through irrigation. A detailed analysis of irrigation and dust emission feedbacks will be the subject of a separate paper.

In Northeast China (region L) emissions have increased since the 1950s, with SO_2 emissions starting to decrease since 2000s, whereas NO_x and NH_3 still increase. Organic carbon emissions in both Northeast China and in Southeast Asia are higher than in any other region studied here and are still on an upward trend, caused by residential use of biomass and other fire emissions, such as agricultural burning. Aerosol loads (Figure 7) show that sulfate is still the dominating aerosol species but in contrast to all other regions outside of Asia, organic aerosol and nitrate play a much stronger role. Both models show an increase in AOD until

2014, the end of the simulation, however they disagree substantially in forcing (Figure 6). This forcing difference, together with the magnitude difference over India, is mainly responsible for the differences seen in the global mean as discussed in section 3.1. MATRIX shows a better simulation in AOD compared to OMA (Fig. 9), but both models underestimate AOD over that region. A comparison of the trend against MODIS is difficult, because of infrequent clear sky conditions in the satellite product, especially during the Summer Monsoon. Both models show an increasing trend of about 0.1 in AOD between 2001 and 2014.

Southeast Asia (region K), which also includes parts of China, has not evidenced a downward trend in emissions by the year 2014 as just discussed further North in China. Here the MATRIX model captures the MODIS AOD in terms of magnitude and variability, showing an increase of 0.1 between 2001 and 2014.

In India (region J) anthropogenic emissions started to rise in the 1950's and emissions are still following an upward trend at the end of the simulated period. India is globally the only region where ammonia plays as an important role as sulfur dioxide. Further, it is the only region worldwide where MATRIX shows a still-increasing trend in RFari(i). MATRIX captures the AOD trend of 0.2 (2001-2014) but underestimates the summer minima in AOD.

3.4 Global change in AOD and radiative fluxes

The slope of the trend between 2001 and 2014, the beginning of MODIS data collection and the end of the CMIP6 historical simulation, for clear sky AOD and shortwave clear-sky outgoing radiation at TOA are shown in Fig 10. The slopes presented are based on the 2001-2014 annual mean data, and have been calculated in two different ways. First, the annual mean of the satellite data, using monthly mean data is calculated. An annual mean data point was calculated even if only one month was available. The slope calculated from these data using a least-squares linear regression methodology is presented in the first row of Fig. 10 a and b. The annual means of the two models were sampled for the same months based on the satellite data availability, and presented in rows 2 (MATRIX) and 3 (OMA) of Fig. 10 c-f. These model slopes are best compared with the satellite, but are missing, depending on location, some months in the annual means. Thus, they do not represent exactly an interannual trend. For this, we use a second method for the two models, using all data, shown in rows 4 (MATRIX) and 5 (OMA) of Fig. 10 g-j. The significance of the simulated trends is calculated by using the slopes per gridbox in all 5 ensemble simulations, and then calculating the variability of the slopes across the ensembles, as the standard deviation over the mean. Figure 10 g-j show results where

the models have less than 50% variability across the ensemble members, area with high variability are marked out grey.

For AOD, the world can be divided into areas of positive and negative trends. Negative trends in aerosol column load that are captured by MODIS and the models are over and downwind the Eastern US, over Central South America and Europe. As seen before, MATRIX simulates larger AOD trends than OMA, while the regional distributions are mostly similar. Negative trends in MODIS that are not captured by the models are seen over Pakistan, Mongolia and the Sahel. The Sahel has experienced a decrease in fire activity in recent years, which is linked to a conversion of land use from Savanna to crop land (Ichoku et al., 2016). Changes in fires and land use also influence desert dust emissions in West Africa (Bauer et al., 2019). The underestimation of biomass burning emissions in the inventory could be responsible for this missing effect in the simulations (Pan et al., 2019). Pakistan shows a strong decreasing trend in MODIS AOD, which we can't explain at the moment (Gupta et al., 2013). Increasing trends in AOD are seen over Northeast China, Siberia, India and the Arabian Peninsula, Central Africa, and the outflow from Central Africa over the Southern Atlantic. The models, especially MATRIX, capture these large-scale features. However, changes in biomass burning plumes in Central Africa are too small, which is consistent with insufficient emissions over Central Africa in the inventory.

We also compared the model simulations against the CERES EBAF data for shortwave clear-sky outgoing radiation at TOA (Fig 10). We add this comparison as an independent dataset to look at trends in regions affected by aerosol changes. The radiation changes are caused by a combination of atmospheric composition changes, such as aerosols and ozone, as well as changes in surface albedo caused by land and ice changes. For example, the strong increase in fluxes around the Antarctic are caused by the change in sea ice cover (King, 2014). However, in this analysis attention should be directed to the areas of largest changes in aerosol load. The best agreement between AOD and radiation trends can be found over the Eastern US. CERES shows a decrease of -1.4 W m^{-2} over the 14-year time period, MATRIX shows -1.9 W m^{-2} and OMA -0.9 W m^{-2}. The increasing trend in the Indian Ocean is also very similar between models and CERES, but the decrease in fluxes over Pakistan, consistent with the reduction of MODIS AOD, is again absent in the models. Overall, CERES and models show a comparable magnitude in radiative flux trend changes, similar to the AOD trends. However, most regions, other than the Eastern US in MATRIX and the Indian ocean in MATRIX and OMA, show very high variability (Fig. 10 h-j), and thus the modeled trends are not be significant. MATRIX

shows a stronger trend in radiative fluxes compared to both CERES and OMA, and it appears to agree with CERES slightly better than OMA, but many regions exhibiting CERES trends are unaccounted for, such as negative trends over the Saharan, Namibian and Australian deserts, and a positive trend over the Middle East.

In summary, the slope difference between models demonstrates that MATRIX has stronger trends compared to OMA, with the best comparison to MODIS or CERES being probably between the two models. The areas where the slopes of AOD and radiation agree the most are where aerosols are the strong players in the radiative distribution, while disagreement in slopes indicates that aerosols are not as important in the radiative distribution over those regions. Alternatively, the model is failing to capture observed aerosol trends (e.g. due to unrealistic emission inventories like for biomass burning over equatorial Africa).

4 Summary of model performance

The OMA model performed a superior simulation of organic aerosol, at least as evaluated over the United States, compared to MATRIX, due to a better simulation of summertime organic aerosol concentrations (Figure 8), which can be credited to the explicit treatment of secondary organic aerosol in OMA (Tsigaridis et al., 2013). Overall the OMA model did show a systematic underestimation of sulfate aerosol, which we tentatively attribute to a too low in-cloud sulfate production. This will be subject of future studies. The black carbon simulation in OMA is very similar to MATRIX, as its lifetime has been adjusted to match the prognostic calculation of BC in MATRIX (Bauer et al., 2013). OMA's nitrate aerosol simulation has greatly improved since CMIP5 (Nazarenko et al., 2017), due to a bug fix (wet removal of ammonia) and now results between OMA and MATRIX are very similar (Mezuman et al., 2016). Sea salt concentrations and forcing show no trend in the historical simulation. Mineral dust does show a decreasing global atmospheric load over time in both models, which after a first analysis can be explained by effects of irrigation (Cook et al., 2015) on dust emissions. In addition, dust coatings by sulfate and nitrate (Bauer et al., 2007; Bauer & Koch, 2005) lead to changes in dust lifetime. Clay and fine silt particles in OMA under pre-industrial conditions had about one-day longer lifetime than at present day due to less sulfate and nitrate coatings that reduce their wet removal rates. Those changes in mineral dust result in a small positive anthropogenic forcing, as the net negative dust direct radiative forcing effect is reduced over time. The preindustrial to present day forcings by composition in OMA are as follows; sulfate

-0.30, nitrate -0.15, organic aerosol -0.06, black carbon 0.22, sea salt 0.00, and dust 0.05 Wm^{-2}, resulting in a total net RFari(i) of -0.24 Wm^{-2}.

The MATRIX model showed a superior simulation of sulfate aerosol and AOD, compared to OMA. In MATRIX sulfate aerosol formation depends in addition to its gas and aqueous phase production rates on new particle formation and growth. Sulfate, as well as all other inorganic aerosols, are distributed over the entire size distribution which impacts aerosol lifetime. In this version of MATRIX organic aerosols are treated as non-volatile, which explains the overestimation of OA in the US during summer months. A scheme including semi-volatile organics has been developed for MATRIX (Gao et al., 2017, 2018) and will be used in future studies. As discussed above, the nitrate simulations between OMA and MATRIX are very similar as both schemes use the thermodynamic equilibrium model EQSAM (Metzger et al., 2002). Sea salt and dust emissions parameterizations and the resulting trends are also shared between the schemes. Forcing numbers per specie are not given for MATRIX, as aerosols are internally mixed.

Simulating aerosol composition is just the first step to calculate forcing. Even if OMA and MATRIX would have identical loads, their aerosol forcing would differ because of three factors: particle size, effective refractive indices (which differ for internal and external mixtures), and aerosol water. Particle size is constant in OMA, while time- and space-varying and depending on particle growth in MATRIX. Refractive indices in OMA only vary for hygroscopic particles with ambient relative humidity, while in MATRIX refractive indices depend on the individual mixing state of each simulated aerosol population (Bauer et al., 2013) and the aerosol water content in each mixing state (Bauer et al., 2010b). Aerosol water, or hygroscopic swelling, is very different in the two models, and we suspect a major contributor to the differences in AOD and forcing. Similarly, the different complexities in microphysical aerosol properties represented in the models, lead to different aerosol – cloud activations and ultimately impact forcing.

5 Conclusions

This study summarizes the aerosol composition simulations of GISS ModelE2.1 which are used as the basis for the GISS CMIP6 (Eyring et al., 2016) coupled simulations with non-interactive atmospheric composition. The monthly mean aerosol time series from 1850 to 2014 are used as input for the non-interactive simulations. The model configuration is used for GISS ModelE2.1 simulations for AerChemMIP (Collins et al., 2017), AeroCom (Textor et al.,

2006)(Schulz et al,, 2009) Phase 3 experiments, and as the starting point for the ScenarioMIP simulations (O'Neill et al., 2016).

In conclusion, this study demonstrates how detailed treatment of aerosol microphysical processes impact forcing and, in this case, even forcing trends. We raised the question in the introduction whether Earth has already reached the maximum negative forcing effects of anthropogenic aerosols on a global basis, the most important forcing that counterbalances GHG warming, and whether this will be even more the case as reduction of local pollution expands across more nations. Our two models show different global forcing trends, both in terms of aerosol direct and indirect forcing, driven by the different magnitude of sulfate versus organic aerosol effects in the two models. The evaluation of the models with surface composition data and satellite AOD and radiative fluxes showed that observations often fall in between the two models. As such, we cannot provide a conclusive answer from this study whether peak global aerosol forcing has already taken place. However, if the MATRIX model is correct, and most regional AOD trend comparisons point to this, then peak aerosol forcing was reached in the 1980s. As a consequence, it could be possible that the recently observed global warming which is primarily driven by greenhouse gases has been augmented by the effect of a decreasing aerosol cooling effect on the global scale. This is of major relevance to the validity of some recent emergent constraints based on recent temperature trends (Njisse et al, 2020, Tokarska et al., 2020). In order to investigate this hypothesis, we are working on a follow-up paper that extends the CMIP6 simulations until present day (as opposed to up to 2014 in this study) as well as making use of the ScenarioMIP (O'Neill et al., 2016) simulations.

Acknowledgments and Data

The authors SEB and KT acknowledge funding from NASA's Atmospheric Composition Modeling and Analysis Program (ACMAP), contract number NNX15AE36G. RLM acknowledges support from the Modeling, Analysis and Prediction Program NNG14HH42I. Resources supporting this work were provided by the NASA High-End Computing (HEC) Program through the NASA Center for Climate Simulation (NCCS) at Goddard Space Flight Center. The model simulations are available at the CMIP6 data portals: USA, PCMDI/LLNL (California) - https://esgf-node.llnl.gov/projects/cmip6/, France, IPSL - https://esgf-node.ipsl.upmc.fr/projects/cmip6-ipsl/, Germany, DKRZ - https://esgf-

data.dkrz.de/projects/cmip6-dkrz/ or UK, CEDA - https://esgf-index1.ceda.ac.uk/projects/cmip6-ceda/

References

Abdul-Razzak, H., & Ghan, S. J. (2000). A parameterization of aerosol activation: 2. Multiple aerosol types. *Journal of Geophysical Research: Atmospheres*, *105*(D5), 6837–6844. https://doi.org/10.1029/1999JD901161

Abdul-Razzak, H., Ghan, S. J., & Rivera-Carpio, C. (1998). A parameterization of aerosol activation: 1. Single aerosol type. *Journal of Geophysical Research: Atmospheres*, *103*(D6), 6123–6131. https://doi.org/10.1029/97JD03735

Adesina, A. J., Kumar, K. R., Sivakumar, V., & Piketh, S. J. (2016). Intercomparison and assessment of long-term (2004-2013) multiple satellite aerosol products over two contrasting sites in South Africa. *JASTP*, *148*, 82–95. https://doi.org/10.1016/j.jastp.2016.09.001

Aklesso, M., Kumar, K. R., Bu, L., & Boiyo, R. (2018). Analysis of spatial-temporal heterogeneity in remotely sensed aerosol properties observed during 2005–2015 over three countries along the Gulf of Guinea Coast in Southern West Africa. *Atmospheric Environment*, *182*, 313–324. https://doi.org/10.1016/j.atmosenv.2018.03.062

Alfaro-Contreras, R., Zhang, J., Reid, J. S., & Christopher, S. (2017). A study of 15-year aerosol optical thickness and direct shortwave aerosol radiative effect trends using MODIS, MISR, CALIOP and CERES. *Atmospheric Chemistry and Physics*, *17*(22), 13849–13868. https://doi.org/10.5194/acp-17-13849-2017

Arfeuille, F., Weisenstein, D., Mack, H., Rozanov, E., Peter, T., & Brönnimann, S. (2014). Volcanic forcing for climate modeling: a new microphysics-based data set covering

years 1600–present. *Climate of the Past*, *10*(1), 359–375. https://doi.org/10.5194/cp-10-359-2014

Arkian, F., & Nicholson, S. (2017). Long-term variations of aerosol optical depth and aerosol radiative forcing over Iran based on satellite and AERONET data. *Environmental Monitoring and Assessment*, *190*. https://doi.org/10.1007/s10661-017-6336-1

Bauer, S. E., & Koch, D. (2005). Impact of heterogeneous sulfate formation at mineral dust surfaces on aerosol loads and radiative forcing in the Goddard Institute for Space Studies general circulation model. *Journal of Geophysical Research: Atmospheres*, *110*(D17). https://doi.org/10.1029/2005JD005870

Bauer, S. E., & Menon, S. (2012). Aerosol direct, indirect, semidirect, and surface albedo effects from sector contributions based on the IPCC AR5 emissions for preindustrial and present-day conditions. *Journal of Geophysical Research: Atmospheres*, *117*(D1). https://doi.org/10.1029/2011JD016816

Bauer, S. E., Mishchenko, M. I., Lacis, A. A., Zhang, S., Perlwitz, J., & Metzger, S. M. (2007). Do sulfate and nitrate coatings on mineral dust have important effects on radiative properties and climate modeling? *Journal of Geophysical Research: Atmospheres*, *112*(D6). https://doi.org/10.1029/2005JD006977

Bauer, S. E., Koch, D., Unger, N., Metzger, S. M., Shindell, D. T., & Streets, D. G. (2007). Nitrate aerosols today and in 2030: a global simulation including aerosols and tropospheric ozone. *Atmospheric Chemistry and Physics*, *7*(19), 5043–5059. https://doi.org/10.5194/acp-7-5043-2007

Bauer, S. E., Wright, D. L., Koch, D., Lewis, E. R., McGraw, R., Chang, L.-S., et al. (2008). MATRIX (Multiconfiguration Aerosol TRacker of mIXing state): an aerosol microphysical module for global atmospheric models. *Atmospheric Chemistry and Physics*, *8*(20), 6003–6035. https://doi.org/10.5194/acp-8-6003-2008

Bauer, S. E., Menon, S., Koch, D., Bond, T. C., & Tsigaridis, K. (2010a). A global modeling study on carbonaceous aerosol microphysical characteristics and radiative effects. *Atmospheric Chemistry and Physics*, *10*(15), 7439–7456. https://doi.org/10.5194/acp-10-7439-2010

Bauer, S. E., Menon, S., Koch, D., Bond, T. C., & Tsigaridis, K. (2010b). A global modeling study on carbonaceous aerosol microphysical characteristics and radiative effects. *Atmospheric Chemistry and Physics*, *10*(15), 7439–7456. https://doi.org/10.5194/acp-10-7439-2010

Bauer, S. E., Ault, A., & Prather, K. A. (2013). Evaluation of aerosol mixing state classes in the GISS modelE-MATRIX climate model using single-particle mass spectrometry measurements. *Journal of Geophysical Research: Atmospheres*, *118*(17), 9834–9844. https://doi.org/10.1002/jgrd.50700

Bauer, S. E., Bausch, A., Nazarenko, L., Tsigaridis, K., Xu, B., Edwards, R., et al. (2013). Historical and future black carbon deposition on the three ice caps: Ice core measurements and model simulations from 1850 to 2100. *Journal of Geophysical Research: Atmospheres*, *118*(14), 7948–7961. https://doi.org/10.1002/jgrd.50612

Bauer, S. E., Im, U., Mezuman, K., & Gao, C. Y. (2019). Desert Dust, Industrialization, and Agricultural Fires: Health Impacts of Outdoor Air Pollution in Africa. *Journal of Geophysical Research: Atmospheres*, *124*(7), 4104–4120. https://doi.org/10.1029/2018JD029336

Bellouin, N., Boucher, O., Haywood, J., & Reddy, M. S. (2005). Global estimate of aerosol direct radiative forcing from satellite measurements. *Nature*, *438*(7071), 1138–1141. https://doi.org/10.1038/nature04348

Bellouin, N., Jones, A., Haywood, J., & Christopher, S. A. (2008). Updated estimate of aerosol direct radiative forcing from satellite observations and comparison against the

Hadley Centre climate model. *Journal of Geophysical Research: Atmospheres*, *113*(D10). https://doi.org/10.1029/2007JD009385

Boiyo, R., Kumar, K. R., & Zhao, T. (2018). Spatial variations and trends in AOD climatology over East Africa during 2002–2016: a comparative study using three satellite data sets. *International Journal of Climatology*, *38*(S1), e1221–e1240. https://doi.org/10.1002/joc.5446

Collins, W. J., Lamarque, J.-F., Schulz, M., Boucher, O., Eyring, V., Hegglin, M. I., et al. (2017). AerChemMIP: quantifying the effects of chemistry and aerosols in CMIP6. *Geoscientific Model Development*, *10*(2), 585–607. https://doi.org/10.5194/gmd-10-585-2017

Cook, B. I., Shukla, S. P., Puma, M. J., & Nazarenko, L. S. (2015). Irrigation as an historical climate forcing. *Climate Dynamics*, *44*(5), 1715–1730. https://doi.org/10.1007/s00382-014-2204-7

Eyring, V., Bony, S., Meehl, G. A., Senior, C. A., Stevens, B., Stouffer, R. J., & Taylor, K. E. (2016). Overview of the Coupled Model Intercomparison Project Phase 6 (CMIP6) experimental design and organization. *Geoscientific Model Development*, *9*(5), 1937–1958. https://doi.org/10.5194/gmd-9-1937-2016

Fan, X., Xia, X., & Chen, H. (2018). Can MODIS detect trends in aerosol optical depth over land? *Advances in Atmospheric Sciences*, *35*(2), 135–145. https://doi.org/10.1007/s00376-017-7017-2

Floutsi, A. A., Korras-Carraca, M. B., Matsoukas, C., Hatzianastassiou, N., & Biskos, G. (2016). Climatology and trends of aerosol optical depth over the Mediterranean basin during the last 12years (2002-2014) based on Collection 006 MODIS-Aqua data. *The Science of the Total Environment*, *551–552*, 292–303. https://doi.org/10.1016/j.scitotenv.2016.01.192

Gao, C. Y., Tsigaridis, K., & Bauer, S. E. (2017). MATRIX-VBS (v1.0): implementing an evolving organic aerosol volatility in an aerosol microphysics model. *Geoscientific Model Development*, *10*(2), 751–764. https://doi.org/10.5194/gmd-10-751-2017

Gao, C. Y., Bauer, S. E., & Tsigaridis, K. (2018). Can semi-volatile organic aerosols lead to fewer cloud particles? *Atmospheric Chemistry and Physics*, *18*(19), 14243–14251. https://doi.org/10.5194/acp-18-14243-2018

Gettelman, A., Hannay, C., Bacmeister, J. T., Neale, R. B., Pendergrass, A. G., Danabasoglu, G., et al. (2019). High Climate Sensitivity in the Community Earth System Model Version 2 (CESM2). *Geophysical Research Letters*, *46*(14), 8329–8337. https://doi.org/10.1029/2019GL083978

Ghan, S. J. (2013). Technical Note: Estimating aerosol effects on cloud radiative forcing. *Atmospheric Chemistry and Physics*, *13*(19), 9971–9974. https://doi.org/10.5194/acp-13-9971-2013

GISS, NASA Goddard Institute for Space Studies (NASA/GISS) **(2019)**. *NASA-GISS GISS-E2-2-G model output prepared for CMIP6 CMIP amip*.Earth System Grid Federation. https://doi.org/10.22033/ESGF/CMIP6.6986

Golaz, J.-C., Caldwell, P. M., Roekel, L. P. V., Petersen, M. R., Tang, Q., Wolfe, J. D., et al. (2019). The DOE E3SM Coupled Model Version 1: Overview and Evaluation at Standard Resolution. *Journal of Advances in Modeling Earth Systems*, *11*(7), 2089–2129. https://doi.org/10.1029/2018MS001603

Gopal, K. R., Obul Reddy, K. R., Balakrishnaiah, G., Arafath, S. M., Kumar Reddy, N. S., Rao, T. C., et al. (2016). Regional trends of aerosol optical depth and their impact on cloud properties over Southern India using MODIS data. *JASTP*, *146*, 38–48. https://doi.org/10.1016/j.jastp.2016.05.005

Gupta, P., Khan, M. N., da Silva, A., & Patadia, F. (2013). MODIS aerosol optical depth observations over urban areas in Pakistan: quantity and quality of the data for air quality monitoring. *Atmospheric Pollution Research*, *4*(1), 43–52. https://doi.org/10.5094/APR.2013.005

Hand, J. L., Schichtel, B. A., Pitchford, M., Malm, W. C., & Frank, N. H. (2012). Seasonal composition of remote and urban fine particulate matter in the United States. *Journal of Geophysical Research: Atmospheres*, *117*(D5). https://doi.org/10.1029/2011JD017122

Hansen, J. E., Sato, M., Lacis, A., Ruedy, R., Tegen, I., & Matthews, E. (1998). Climate forcings in the Industrial era. *Proceedings of the National Academy of Sciences*, *95*(22), 12753–12758. https://doi.org/10.1073/pnas.95.22.12753

He, Q., Zhang, M., & Huang, B. (2016). Spatio-temporal variation and impact factors analysis of satellite-based aerosol optical depth over China from 2002 to 2015. *Atmospheric Environment*, *129*, 79–90. https://doi.org/10.1016/j.atmosenv.2016.01.002

Held, I. M., Guo, H., Adcroft, A., Dunne, J. P., Horowitz, L. W., Krasting, J., et al. (2020). Structure and Performance of GFDL's CM4.0 Climate Model. *Journal of Advances in Modeling Earth Systems*, *n/a*(n/a). https://doi.org/10.1029/2019MS001829

Herren, P.-A., Eichler, A., Machguth, H., Papina, T., Tobler, L., Zapf, A., & Schwikowski, M. (2013). The onset of Neoglaciation 6000 years ago in western Mongolia revealed by an ice core from the Tsambagarav mountain range. *Quaternary Science Reviews*, *69*, 59–68. https://doi.org/10.1016/j.quascirev.2013.02.025

Hoesly, R. M., Smith, S. J., Feng, L., Klimont, Z., Janssens-Maenhout, G., Pitkanen, T., et al. (2018). Historical (1750–2014) anthropogenic emissions of reactive gases and

aerosols from the Community Emissions Data System (CEDS). *Geoscientific Model Development*, *11*(1), 369–408. https://doi.org/10.5194/gmd-11-369-2018

Hu, K., Kumar, K. R., Kang, N., Boiyo, R., & Wu, J. (2018). Spatiotemporal characteristics of aerosols and their trends over mainland China with the recent Collection 6 MODIS and OMI satellite datasets. *Environmental Science and Pollution Research*, *25*(7), 6909–6927. https://doi.org/10.1007/s11356-017-0715-6

Ichoku, C., Ellison, L. T., Willmot, K. E., Matsui, T., Dezfuli, A. K., Gatebe, C. K., et al. (2016). Biomass burning, land-cover change, and the hydrological cycle in Northern sub-Saharan Africa. *Environmental Research Letters*, *11*(9), 095005. https://doi.org/10.1088/1748-9326/11/9/095005

Jenk, T. M., Szidat, S., Bolius, D., Sigl, M., Gäggeler, H. W., Wacker, L., et al. (2009). A novel radiocarbon dating technique applied to an ice core from the Alps indicating late Pleistocene ages. *Journal of Geophysical Research: Atmospheres*, *114*(D14). https://doi.org/10.1029/2009JD011860

Jongeward, A. R., Li, Z., He, H., & Xiong, X. (2016). Natural and Anthropogenic Aerosol Trends from Satellite and Surface Observations and Model Simulations over the North Atlantic Ocean from 2002 to 2012. *Journal of the Atmospheric Sciences*, *73*(11), 4469–4485. https://doi.org/10.1175/JAS-D-15-0308.1

Keegan, K. M., Albert, M. R., McConnell, J. R., & Baker, I. (2014). Climate change and forest fires synergistically drive widespread melt events of the Greenland Ice Sheet. *Proceedings of the National Academy of Sciences*, *111*(22), 7964–7967. https://doi.org/10.1073/pnas.1405397111

King, J. (2014). A resolution of the Antarctic paradox. *Nature*, *505*(7484), 491–492. https://doi.org/10.1038/505491a

Koch, D., Jacob, D., Tegen, I., Rind, D., & Chin, M. (1999). Tropospheric sulfur simulation and sulfate direct radiative forcing in the Goddard Institute for Space Studies general circulation model. *Journal of Geophysical Research: Atmospheres, 104*(D19), 23799–23822. https://doi.org/10.1029/1999JD900248

Koch, D., Schmidt, G. A., & Field, C. V. (2006). Sulfur, sea salt, and radionuclide aerosols in GISS ModelE. *Journal of Geophysical Research: Atmospheres, 111*(D6). https://doi.org/10.1029/2004JD005550

Kumar, M., Parmar, K. S., Kumar, D. B., Mhawish, A., Broday, D. M., Mall, R. K., & Banerjee, T. (2018). Long-term aerosol climatology over Indo-Gangetic Plain: Trend, prediction and potential source fields. *Atmospheric Environment, 180*, 37–50. https://doi.org/10.1016/j.atmosenv.2018.02.027

Lamarque, J.-F., Bond, T. C., Eyring, V., Granier, C., Heil, A., Klimont, Z., et al. (2010). Historical (1850–2000) gridded anthropogenic and biomass burning emissions of reactive gases and aerosols: methodology and application. *Atmospheric Chemistry and Physics*, *10*(15), 7017–7039. https://doi.org/10.5194/acp-10-7017-2010

Levy, R. C., Remer, L. A., Kleidman, R. G., Mattoo, S., Ichoku, C., Kahn, R., & Eck, T. F. (2010). Global evaluation of the Collection 5 MODIS dark-target aerosol products over land. *Atmospheric Chemistry and Physics*, *10*(21), 10399–10420. https://doi.org/10.5194/acp-10-10399-2010

Levy, R. C., Mattoo, S., Munchak, L. A., Remer, L. A., Sayer, A. M., Patadia, F., & Hsu, N. C. (2013). The Collection 6 MODIS aerosol products over land and ocean. *Atmospheric Measurement Techniques*, *6*(11), 2989–3034. https://doi.org/10.5194/amt-6-2989-2013

Levy, R. C., Munchak, L. A., Mattoo, S., Patadia, F., Remer, L. A., & Holz, R. E. (2015). Towards a long-term global aerosol optical depth record: applying a consistent

aerosol retrieval algorithm to MODIS and VIIRS-observed reflectance. *Atmospheric Measurement Techniques*, *8*(10), 4083–4110. https://doi.org/10.5194/amt-8-4083-2015

Lewis, E. R., & Schwartz, S. E. (2013). Sea Salt Aerosol Production Fluxes: Estimates and Critical Analysis. In *Sea Salt Aerosol Production: Mechanisms, Methods, Measurements and Models* (pp. 299–344). American Geophysical Union (AGU). https://doi.org/10.1002/9781118666050.ch5

Lim, S., Faïn, X., Ginot, P., Mikhalenko, V., Kutuzov, S., Paris, J.-D., et al. (2017). Black carbon variability since preindustrial times in the eastern part of Europe reconstructed from Mt. Elbrus, Caucasus, ice cores. *Atmospheric Chemistry and Physics*, *17*(5), 3489–3505. https://doi.org/10.5194/acp-17-3489-2017

Loeb, N. G., Doelling, D. R., Wang, H., Su, W., Nguyen, C., Corbett, J. G., et al. (2018). Clouds and the Earth's Radiant Energy System (CERES) Energy Balanced and Filled (EBAF) Top-of-Atmosphere (TOA) Edition-4.0 Data Product. *Journal of Climate*, *31*(2), 895–918. https://doi.org/10.1175/JCLI-D-17-0208.1

Malm, W. C., Sisler, J. F., Huffman, D., Eldred, R. A., & Cahill, T. A. (1994). Spatial and seasonal trends in particle concentration and optical extinction in the United States. *Journal of Geophysical Research: Atmospheres*, *99*(D1), 1347–1370. https://doi.org/10.1029/93JD02916

Malm, W. C., Schichtel, B. A., Pitchford, M. L., Ashbaugh, L. L., & Eldred, R. A. (2004). Spatial and monthly trends in speciated fine particle concentration in the United States. *Journal of Geophysical Research: Atmospheres*, *109*(D3). https://doi.org/10.1029/2003JD003739

van Marle, M. J. E., Kloster, S., Magi, B. I., Marlon, J. R., Daniau, A.-L., Field, R. D., et al. (2017). Historic global biomass burning emissions for CMIP6 (BB4CMIP) based on

merging satellite observations with proxies and fire models (1750–2015). *Geoscientific Model Development*, *10*(9), 3329–3357. https://doi.org/10.5194/gmd-10-3329-2017

Mehta, M., Singh, N., & Anshumali. (2018). Global trends of columnar and vertically distributed properties of aerosols with emphasis on dust, polluted dust and smoke - inferences from 10-year long CALIOP observations. *Remote Sensing of Environment*, *208*, 120–132. https://doi.org/10.1016/j.rse.2018.02.017

Menon, S., & Rotstayn, L. (2006). The radiative influence of aerosol effects on liquid-phase cumulus and stratiform clouds based on sensitivity studies with two climate models. *Climate Dynamics*, *27*(4), 345–356. https://doi.org/10.1007/s00382-006-0139-3

Menon, S., Unger, N., Koch, D., Francis, J., Garrett, T., Sednev, I., et al. (2008). Aerosol climate effects and air quality impacts from 1980 to 2030. *Environmental Research Letters*, *3*(2), 024004. https://doi.org/10.1088/1748-9326/3/2/024004

Menon, S., Koch, D., Beig, G., Sahu, S., Fasullo, J., & Orlikowski, D. (2010). Black carbon aerosols and the third polar ice cap. *Atmospheric Chemistry and Physics*, *10*(10), 4559–4571. https://doi.org/10.5194/acp-10-4559-2010

Metzger, S., Dentener, F., Pandis, S., & Lelieveld, J. (2002). Gas/aerosol partitioning: 1. A computationally efficient model. *Journal of Geophysical Research: Atmospheres*, *107*(D16), ACH 16-1-ACH 16-24. https://doi.org/10.1029/2001JD001102

Mezuman, K., Bauer, S. E., & Tsigaridis, K. (2016). Evaluating secondary inorganic aerosols in three dimensions. *Atmospheric Chemistry and Physics*, *16*(16), 10651–10669. https://doi.org/10.5194/acp-16-10651-2016

Mezuman, K., Tsigaridis, K., Faluvegi, G., & Bauer, S. E. (2019). The interactive global fire module pyrE. *Geoscientific Model Development Discussions*, 1–58. https://doi.org/10.5194/gmd-2019-263

Miller, R. L., Cakmur, R. V., Perlwitz, J., Geogdzhayev, I. V., Ginoux, P., Koch, D., et al. (2006). Mineral dust aerosols in the NASA Goddard Institute for Space Sciences ModelE atmospheric general circulation model. *Journal of Geophysical Research: Atmospheres*, *111*(D6). https://doi.org/10.1029/2005JD005796

Myhre, G., Samset, B. H., Schulz, M., Balkanski, Y., Bauer, S., Berntsen, T. K., et al. (2013). Radiative forcing of the direct aerosol effect from AeroCom Phase II simulations. *Atmospheric Chemistry and Physics*, *13*(4), 1853–1877. https://doi.org/10.5194/acp-13-1853-2013

Myhre, G., D. Shindell, F.-M. Bréon, W. Collins, J. Fuglestvedt, J. Huang, D. Koch, J.-F. Lamarque, D. Lee, B. Mendoza, T. Nakajima, A. Robock, G. Stephens, T. Takemura and H. Zhang, 2013: Anthropogenic and Natural Radiative Forc- ing. In: *Climate Change 2013: The Physical Science Basis. Contribution of Working Group I to the Fifth Assessment Report of the Intergovernmental Panel on Climate Change* [Stocker, T.F., D. Qin, G.-K. Plattner, M. Tignor, S.K. Allen, J. Boschung, A. Nauels, Y. Xia, V. Bex and P.M. Midgley (eds.)]. Cambridge University Press, Cambridge, United Kingdom and New York, NY, USA.

Myhre, G., Aas, W., Cherian, R., Collins, W., Faluvegi, G., Flanner, M., et al. (2017). Multi-model simulations of aerosol and ozone radiative forcing due to anthropogenic emission changes during the period 1990–2015. *Atmospheric Chemistry and Physics*, *17*(4), 2709–2720. https://doi.org/10.5194/acp-17-2709-2017

Nazarenko, L., Rind, D., Tsigaridis, K., Genio, A. D. D., Kelley, M., & Tausnev, N. (2017). Interactive nature of climate change and aerosol forcing. *Journal of Geophysical Research: Atmospheres*, *122*(6), 3457–3480. https://doi.org/10.1002/2016JD025809

Nijsse, F. J. M. M., Cox, P. M., and Williamson, M. S.: An emergent constraint on Transient Climate Response from simulated historical warming in CMIP6 models, Earth Syst. Dynam. Discuss., https://doi.org/10.5194/esd-2019-86, 2020.

Oikawa, E., Nakajima, T., & Winker, D. (2018). An Evaluation of the Shortwave Direct Aerosol Radiative Forcing Using CALIOP and MODIS Observations. *Journal of Geophysical Research: Atmospheres*, *123*(2), 1211–1233. https://doi.org/10.1002/2017JD027247

O'Neill, B. C., Tebaldi, C., Vuuren, D. P. van, Eyring, V., Friedlingstein, P., Hurtt, G., et al. (2016). The Scenario Model Intercomparison Project (ScenarioMIP) for CMIP6. *Geoscientific Model Development*, *9*(9), 3461–3482. https://doi.org/10.5194/gmd-9-3461-2016

Osmont, D., Wendl, I. A., Schmidely, L., Sigl, M., Vega, C. P., Isaksson, E., & Schwikowski, M. (2018). An 800-year high-resolution black carbon ice core record from Lomonosovfonna, Svalbard. *Atmospheric Chemistry and Physics*, *18*(17), 12777–12795. https://doi.org/10.5194/acp-18-12777-2018

Pan, X., Ichoku, C., Chin, M., Bian, H., Darmenov, A., Colarco, P., et al. (2019). Six Global Biomass Burning Emission Datasets: Inter-comparison and Application in one Global Aerosol Model. *Atmospheric Chemistry and Physics Discussions*, 1–39. https://doi.org/10.5194/acp-2019-475

Paulot, F., Paynter, D., Ginoux, P., Naik, V., & Horowitz, L. W. (2018). Changes in the aerosol direct radiative forcing from 2001 to 2015: observational constraints and regional mechanisms. *Atmospheric Chemistry and Physics*, *18*(17), 13265–13281. https://doi.org/10.5194/acp-18-13265-2018

Perlwitz, J. P., Pérez García-Pando, C., & Miller, R. L. (2015a). Predicting the mineral composition of dust aerosols – Part 1: Representing key processes. *Atmospheric*

Chemistry and Physics, *15*(20), 11593–11627. https://doi.org/10.5194/acp-15-11593-2015

Perlwitz, J. P., Pérez García-Pando, C., & Miller, R. L. (2015b). Predicting the mineral composition of dust aerosols – Part 2: Model evaluation and identification of key processes with observations. *Atmospheric Chemistry and Physics*, *15*(20), 11629–11652. https://doi.org/10.5194/acp-15-11629-2015

Rayner, N. A., Parker, D. E., Horton, E. B., Folland, C. K., Alexander, L. V., Rowell, D. P., et al. (2003). Global analyses of sea surface temperature, sea ice, and night marine air temperature since the late nineteenth century. *Journal of Geophysical Research: Atmospheres*, *108*(D14). https://doi.org/10.1029/2002JD002670

Sayer, A. M., & Knobelspiesse, K. D. (2019). How should we aggregate data? Methods accounting for the numerical distributions, with an assessment of aerosol optical depth. *Atmospheric Chemistry and Physics Discussions*, 1–36. https://doi.org/10.5194/acp-2019-372

Sayer, A. M., Munchak, L. A., Hsu, N. C., Levy, R. C., Bettenhausen, C., & Jeong, M.-J. (2014). MODIS Collection 6 aerosol products: Comparison between Aqua's e-Deep Blue, Dark Target, and "merged" data sets, and usage recommendations. *Journal of Geophysical Research: Atmospheres*, *119*(24), 13,965-13,989. https://doi.org/10.1002/2014JD022453

Schmidt, G. A., Kelley, M., Nazarenko, L., Ruedy, R., Russell, G. L., Aleinov, I., et al. (2014). Configuration and assessment of the GISS ModelE2 contributions to the CMIP5 archive. *Journal of Advances in Modeling Earth Systems*, *6*(1), 141–184. https://doi.org/10.1002/2013MS000265

Schwarz, J. P., Gao, R. S., Fahey, D. W., Thomson, D. S., Watts, L. A., Wilson, J. C., et al. (2006). Single-particle measurements of midlatitude black carbon and light-scattering

aerosols from the boundary layer to the lower stratosphere. *Journal of Geophysical Research: Atmospheres*, *111*(D16). https://doi.org/10.1029/2006JD007076

Sellar, A. A., Jones, C. G., Mulcahy, J., Tang, Y., Yool, A., Wiltshire, A., et al. (n.d.). UKESM1: Description and evaluation of the UK Earth System Model. *Journal of Advances in Modeling Earth Systems*, *n/a*(n/a). https://doi.org/10.1029/2019MS001739

Shindell, D. , T, Faluvegi, G., Unger, N., Aguilar, E., Schmidt, G. , et al. (2006). Simulations of preindustrial, present-day, and 2100 conditions in the NASA GISS composition and climate model G-PUCCINI. *Atmospheric Chemistry and Physics*, *6*(12), 4427–4459. https://doi.org/10.5194/acp-6-4427-2006

Shindell, D. T., Grenfell, J. L., Rind, D., Grewe, V., & Price, C. (2001). Chemistry-climate interactions in the Goddard Institute for Space Studies general circulation model: 1. Tropospheric chemistry model description and evaluation. *Journal of Geophysical Research: Atmospheres*, *106*(D8), 8047–8075. https://doi.org/10.1029/2000JD900704

Shindell, D. T., Faluvegi, G., & Bell, N. (2003). Preindustrial-to-present-day radiative forcing by tropospheric ozone from improved simulations with the GISS chemistry-climate GCM. *Atmospheric Chemistry and Physics*, *3*(5), 1675–1702. https://doi.org/10.5194/acp-3-1675-2003

Shokr, M., El-Tahan, M., Ibrahim, A., Steiner, A., & Gad, N. (2017). Long-Term, High-Resolution Survey of Atmospheric Aerosols over Egypt with NASA's MODIS Data. *Remote Sensing*, *9*(10), 1027. https://doi.org/10.3390/rs9101027

Sigl, M., McConnell, J. R., Layman, L., Maselli, O., McGwire, K., Pasteris, D., et al. (2013). A new bipolar ice core record of volcanism from WAIS Divide and NEEM and implications for climate forcing of the last 2000 years. *Journal of Geophysical Research: Atmospheres*, *118*(3), 1151–1169. https://doi.org/10.1029/2012JD018603

Sigl, M., Abram, N. J., Gabrieli, J., Jenk, T. M., Osmont, D., & Schwikowski, M. (2018). 19th century glacier retreat in the Alps preceded the emergence of industrial black carbon deposition on high-alpine glaciers. *The Cryosphere*, *12*(10), 3311–3331. https://doi.org/10.5194/tc-12-3311-2018

Su, W., Loeb, N. G., Schuster, G. L., Chin, M., & Rose, F. G. (2013). Global all-sky shortwave direct radiative forcing of anthropogenic aerosols from combined satellite observations and GOCART simulations. *Journal of Geophysical Research: Atmospheres*, *118*(2), 655–669. https://doi.org/10.1029/2012JD018294

Tang, I. N., & Munkelwitz, H. R. (1994). Aerosol Phase Transformation and Growth in the Atmosphere. *Journal of Applied Meteorology*, *33*(7), 791–796. https://doi.org/10.1175/1520-0450(1994)033<0791:APTAGI>2.0.CO;2

Tegen, I., & Fung, I. (1994). Modeling of mineral dust in the atmosphere: Sources, transport, and optical thickness. *Journal of Geophysical Research: Atmospheres*, *99*(D11), 22897–22914. https://doi.org/10.1029/94JD01928

Textor, C., Schulz, M., Guibert, S., Kinne, S., Balkanski, Y., Bauer, S., et al. (2006). Analysis and quantification of the diversities of aerosol life cycles within AeroCom. *Atmospheric Chemistry and Physics*, *6*, 1777–1813. https://doi.org/10.5194/acp-6-1777-2006

Thomason, L. W., Ernest, N., Millán, L., Rieger, L., Bourassa, A., Vernier, J.-P., et al. (2018). A global space-based stratospheric aerosol climatology: 1979–2016. *Earth System Science Data*, *10*(1), 469–492. https://doi.org/10.5194/essd-10-469-2018

Tokarska K.B., M. B. Stolpe, S. Sippel, E. M. Fischer, C. J. Smith, F. Lehner, R. Knutti, Past warming trend constrains future warming in CMIP6 models. *Sci. Adv.* **6**, eaaz9549 (2020).

Tsigaridis, K., & Kanakidou, M. (2003). Global modelling of secondary organic aerosol in the troposphere: a sensitivity analysis. *Atmospheric Chemistry and Physics*, *3*(5), 1849–1869. https://doi.org/10.5194/acp-3-1849-2003

Tsigaridis, K., Koch, D., & Menon, S. (2013). Uncertainties and importance of sea spray composition on aerosol direct and indirect effects. *Journal of Geophysical Research: Atmospheres*, *118*(1), 220–235. https://doi.org/10.1029/2012JD018165

Tsigaridis, K., Daskalakis, N., Kanakidou, M., Adams, P.J., Artaxo, P., Bahadur, R., Balkanski, Y., Bauer S.E., et al. (2014). The AeroCom evaluation and intercomparison of organic aerosol in global models *Atmos. Chem. Phys.*, **14**, 10845-10895, doi:10.5194/acp-14-10845-2014.

Vehkamäki, H., Kulmala, M., Napari, I., Lehtinen, K. E. J., Timmreck, C., Noppel, M., & Laaksonen, A. (2002). An improved parameterization for sulfuric acid–water nucleation rates for tropospheric and stratospheric conditions. *Journal of Geophysical Research: Atmospheres*, *107*(D22), AAC 3-1-AAC 3-10. https://doi.org/10.1029/2002JD002184

Voldoire, A., Saint-Martin, D., Sénési, S., Decharme, B., Alias, A., Chevallier, M., et al. (2019). Evaluation of CMIP6 DECK Experiments With CNRM-CM6-1. *Journal of Advances in Modeling Earth Systems*, *11*(7), 2177–2213. https://doi.org/10.1029/2019MS001683

Wang, P., Ning, S., Dai, J., Sun, J., Lv, M., Song, Q., et al. (2017). Trends and Variability in Aerosol Optical Depth over North China from MODIS C6 Aerosol Products during 2001–2016. *Atmosphere*, *8*(11), 223. https://doi.org/10.3390/atmos8110223

Wang, Z., Shao, M., Chen, L., Tao, M., Zhong, L., Chen, D., et al. (2016). Space view of the decadal variation for typical air pollutants in the Pearl River Delta (PRD) region in

China. *Frontiers of Environmental Science & Engineering*, *10*(5), 9. https://doi.org/10.1007/s11783-016-0853-y

van der Werf, G. R., Randerson, J. T., Giglio, L., Leeuwen, T. T. van, Chen, Y., Rogers, B. M., et al. (2017). Global fire emissions estimates during 1997–2016. *Earth System Science Data*, *9*(2), 697–720. https://doi.org/10.5194/essd-9-697-2017

Wielicki, B. A., Barkstrom, B. R., Baum, B. A., Charlock, T. P., Green, R. N., Kratz, D. P., et al. (1998). Clouds and the Earth's Radiant Energy System (CERES): algorithm overview. *IEEE Transactions on Geoscience and Remote Sensing*, *36*(4), 1127–1141. https://doi.org/10.1109/36.701020

Xu, X., Qiu, J., Xia, X., Sun, L., & Min, M. (2015). Characteristics of atmospheric aerosol optical depth variation in China during 1993–2012. *Atmospheric Environment*, *119*, 82–94. https://doi.org/10.1016/j.atmosenv.2015.08.042

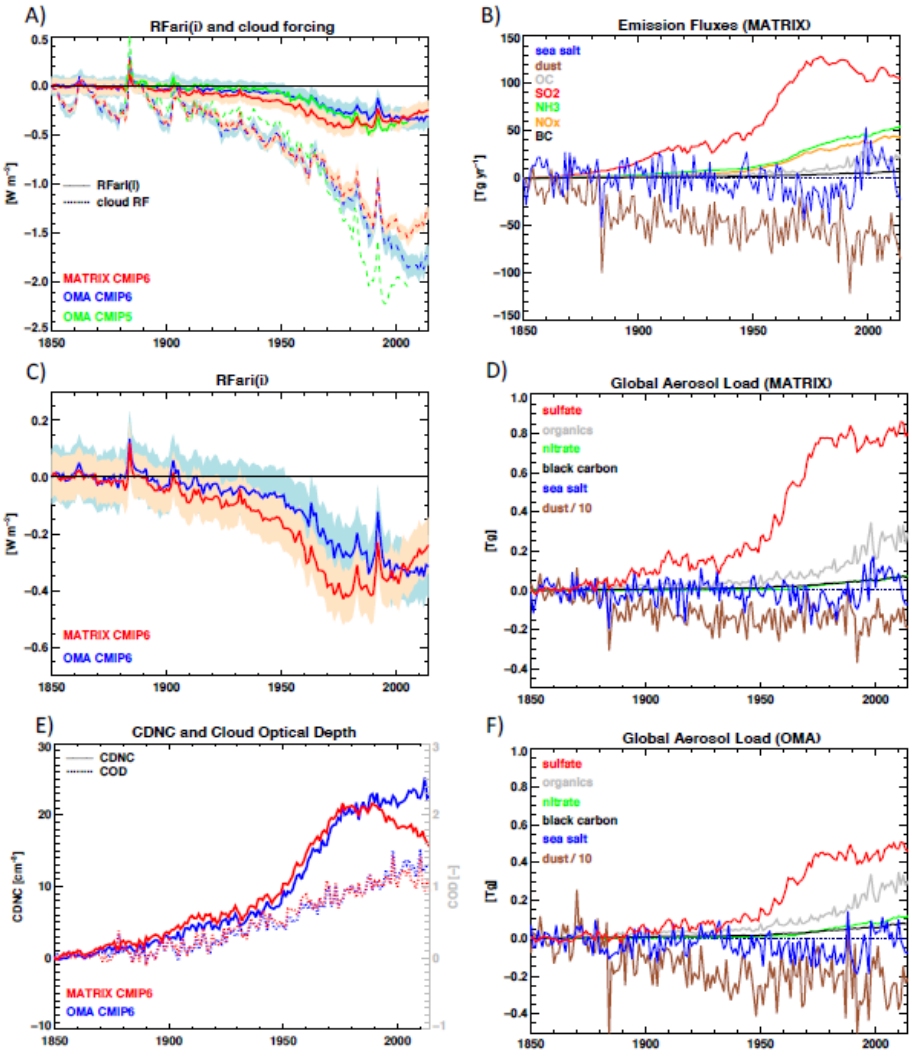

Figure 1. Global mean time series (lines) and 1-sigma range across 5 ensemble members (shaded areas). A) TOA instantaneous tropospheric aerosol forcing RFari(i) (solid lines) and cloud forcing (dashed) for the three model simulations: MATRIX and OMA in the CMIP6 configuration (climate model, emissions and forcing), and OMA from CMIP5. B) Global emission flux anomalies in reference to 1850 for SO_2, NH_3, NO_x, OC, BC, dust and sea salt. C) RFari(i). D) Global column load changes since 1850 of aerosol species for MATRIX, and F) OMA. E) Global mean cloud droplet number concentration (CDNC) and cloud optical depth (COD) changes since 1850.

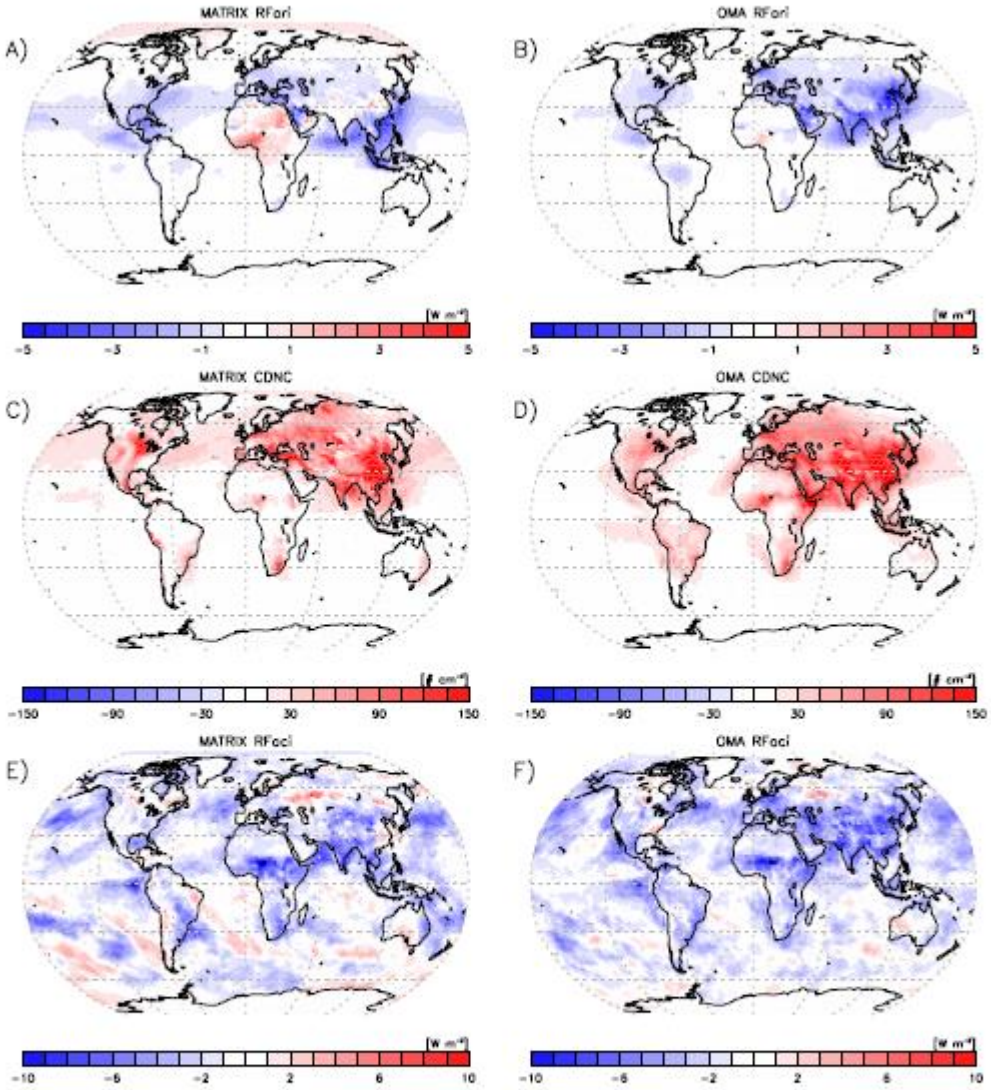

Figure 2 Maps of differences between preindustrial (1850-1859) and present day (2005-2014) aerosol conditions for RFari [W m^{-2}] (top row), CDNC [# cm^{-3}] (middle row) and RFaci [W m^{-2}] (lower panels), for MATRIX (left column) and OMA (right column).

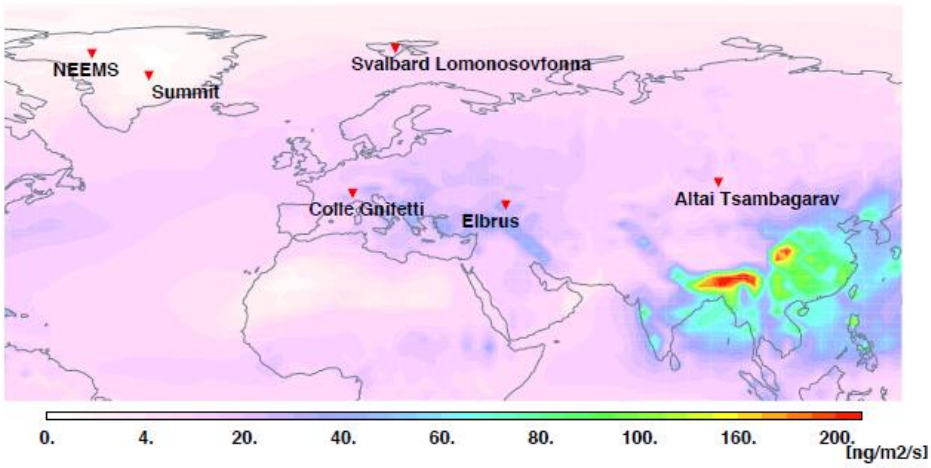

Figure 3 Annual mean map of the sum of dry and wet sulfate deposition fluxes in [ng m^{-2} s^{-1}] for the year 2014. Red triangles indicate the locations of the six ice cores used in figures 4 and 5.

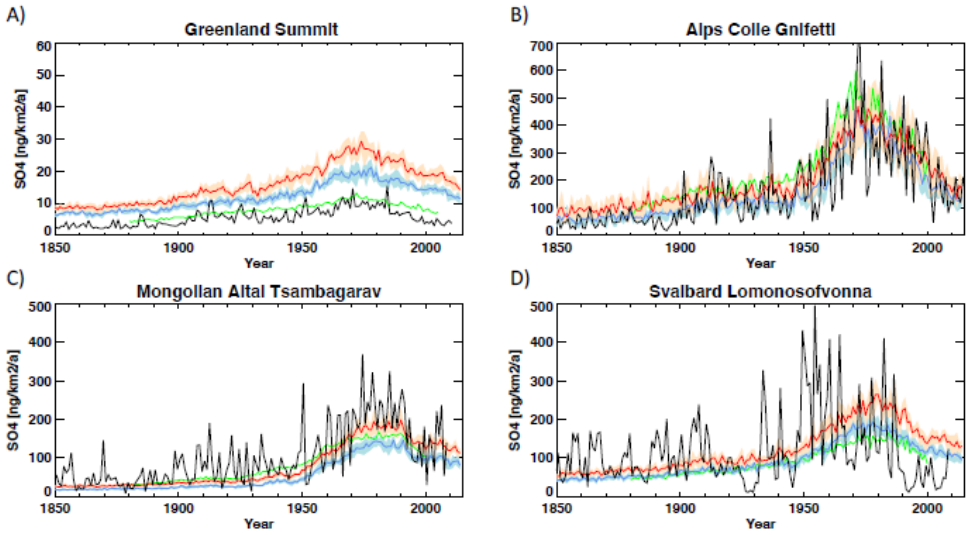

Figure 4 Total sulfate deposition fluxes [ng km^{-2} a^{-1}] for ice cores from Summit in Greenland, Colle Gnifetti in the European Alps, Altai Tsambagarav in Mongolia, and Svalbard Lomonosovfonna. Ice core values (black), MATRIX (red), OMA (blue) from CMIP6 and OMA (green) from CMIP5. Shading indicates the 1-sigma range across the 5 ensemble members.

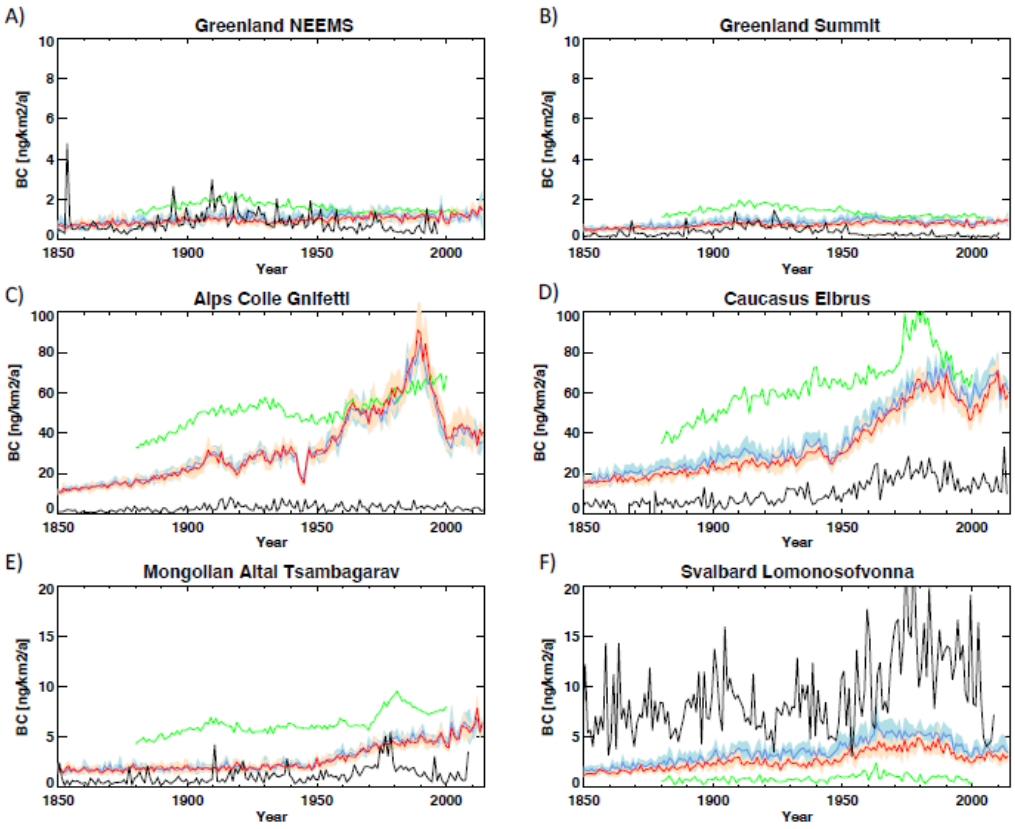

Figure 5 Black carbon deposition fluxes [ng km^{-2} a^{-1}] for ice cores NEEMS and Summit in Greenland, Colle Gnifetti in the European Alps (dashed line show BC fluxes multiplied by 10), Elbrus in the Caucasus, Altai Tsambagarav in Mongolia, and Svalbard Lomonosofvonna. Ice core values (black), MATRIX (red), OMA (blue) from CMIP6 and OMA (green) from CMIP5. Shading indicates the 1-sigma range across the 5 ensemble members.

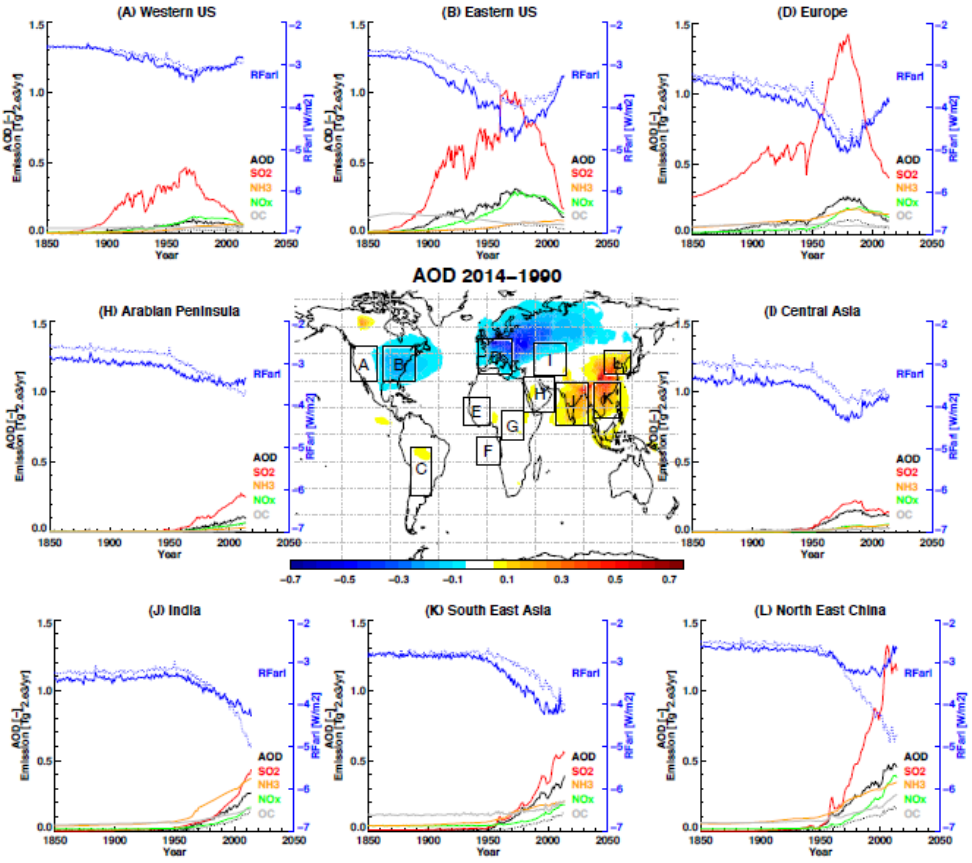

Figure 6 Regional time series from 1850 to 2014 of emissions (NH_3, NO_x, SO_2, OC) in [Tg*2000 yr^{-1}], AOD (black) (left y-axis) and aerosol direct RFari(i) (blue) (right y-axis) from the total aerosols simulated by MATRIX (solid lines) and OMA (dotted lines). The central panel shows the AOD change in MATRIX between 1990 and 2014 and the boxed regions used in this study.

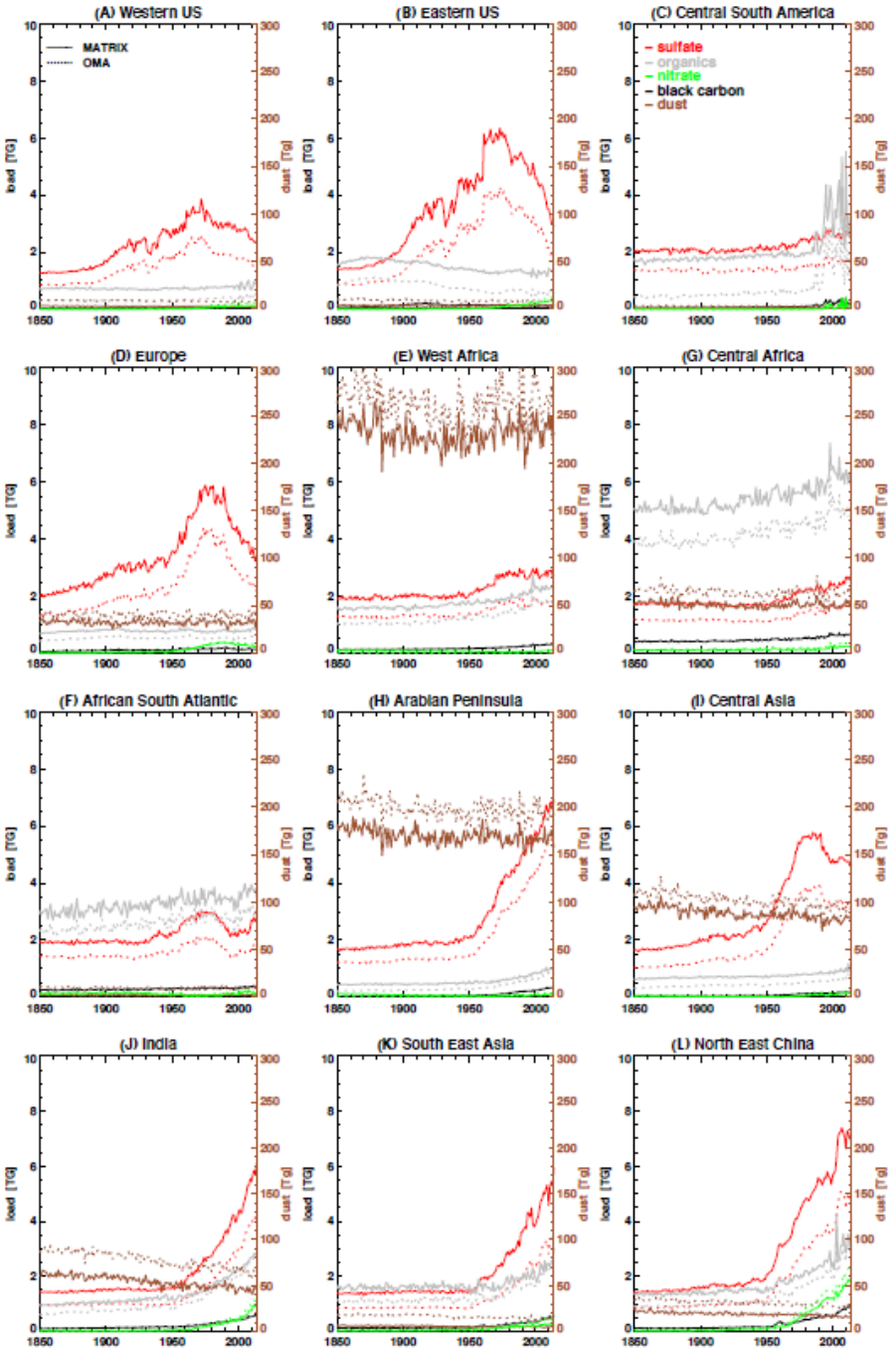

Figure 7 Time series of aerosol mass loading in [Tg] for MATRIX (solid lines) and OMA (dotted) as averaged for boxed regions as indicated in Figure 6. Sulfate (red), organics (grey), nitrate (green) and black carbon (black) loads correspond to the left y-axis, dust loads (brown) to the right y-axis.

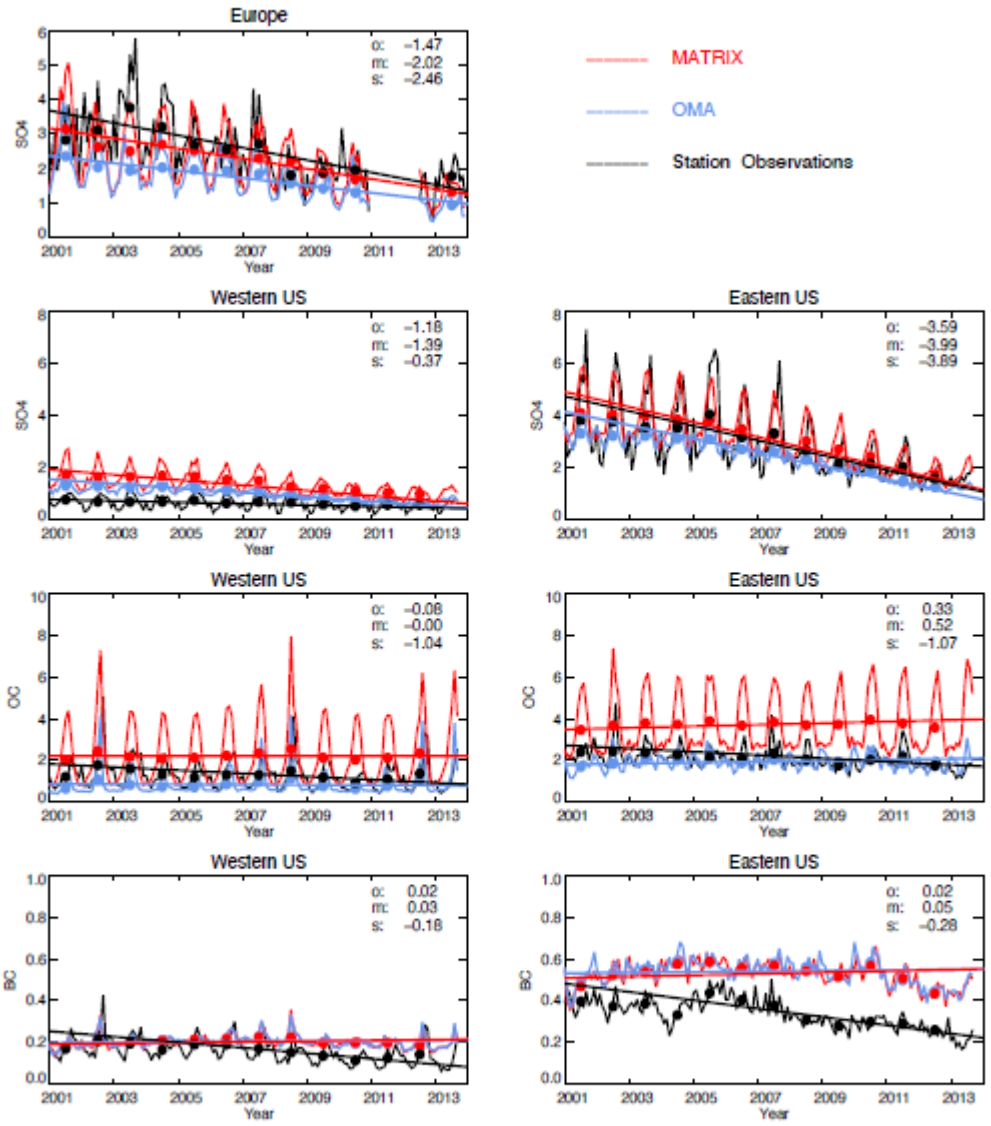

Figure 8 Time series of regional mean surface concentrations [$\mu g\ m^{-3}$] (regions as indicated in Fig. 6) as measured by the IMPROVE (US) and EMEP (Europe) network (black), for Sulfate (top two rows), organic (third row) and black carbon (bottom row). MATRIX (red) and OMA (blue) simulations are sampled according to the spatial and temporal availability of the observations. The straight lines as well as the numbers give the slope of OMA (o), MATRIX (m) and the station data (s). The slope is calculated using a linear regression based on the annual mean (colored dots).

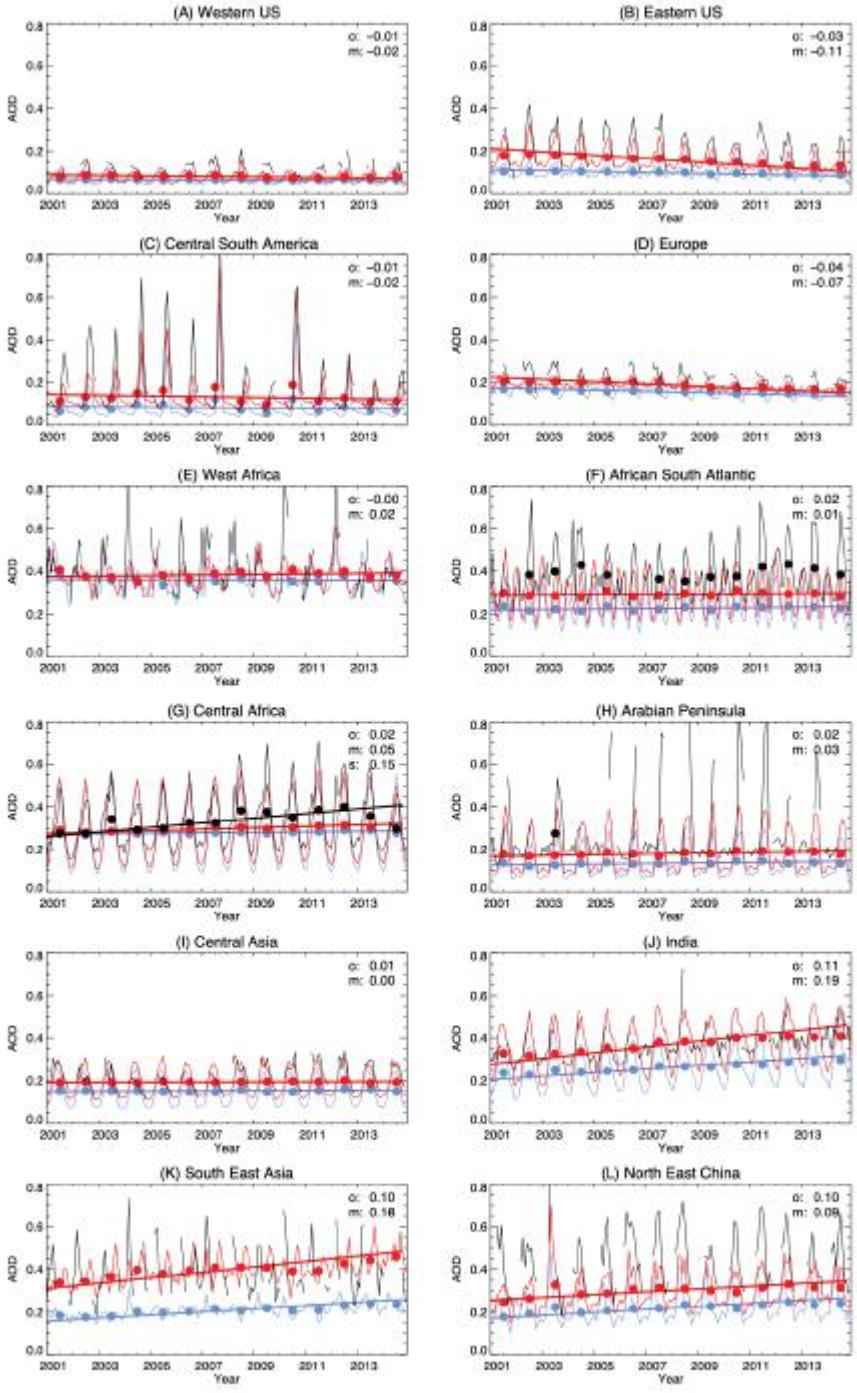

Figure 9 Time series of clear sky AOD for regions as indicated in Fig 6, for MODIS (black), MATRIX (red) and OMA (blue) from 2001 to 2014. The straight lines as well as the numbers give the slope of OMA (o), MATRIX (m) and the satellite data (s). The slope is calculated using a linear regression based on the annual mean (colored dots).

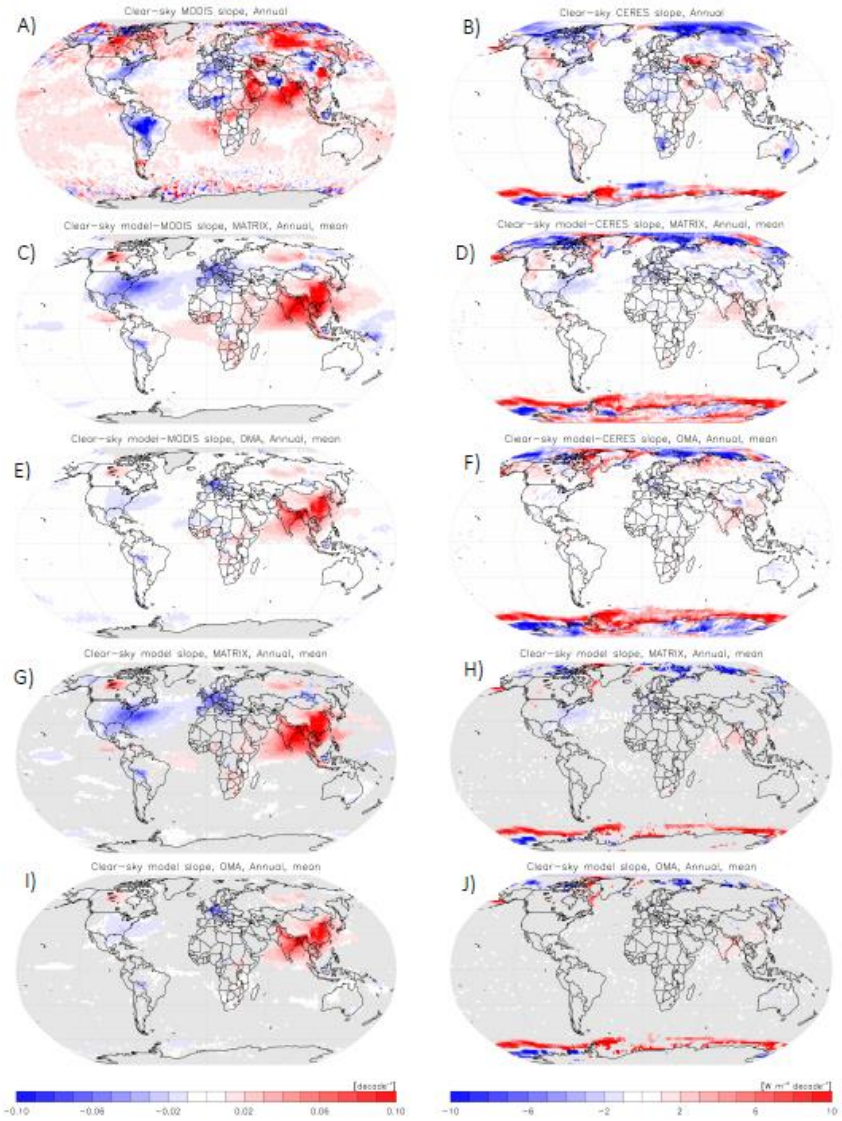

Figure 10 Transient slope between 2001 and 2014 for clear sky AOD [decade^{-1}] in the left column and shortwave top of the atmosphere clear sky flux [W m^{-2} decade^{-1}] in the right column as measured by the satellites (top row; MODIS (left), CERES (right)) and simulated by the models. Second and third rows show MATRIX and OMA, respectively, sampled based on satellite data availability, while 4th and 5th rows show MATRIX and OMA, respectively, using all monthly mean data, regardless of satellite availability. Grey areas in the top three rows represent missing satellite data for all months and in the bottom two rows where the correlation variability across the 5 ensemble simulations (defined as standard deviation over mean) is greater than 50%.